Strain-Rate-Dependent Tensile Response of an Alumina Ceramic: Experiments and Modelling

Jie Zheng[a,*], Haoyang Li[a], James D. Hogan[a]

[a]*Department of Mechanical Engineering, University of Alberta, Edmonton, AB T6G 2R3, Canada.*

Abstract

The strain-rate-dependent tensile response of a commercial alumina ceramic (CeramTec 98% alumina) is investigated by experimental and modelling methods. The experiments at different loading rates are carried out on a standard MTS machine and a modified split-Hopkinson pressure bar system with flattened Brazilian disk specimens. High-speed imaging coupled with digital image correlation (DIC) is used to measure the strain fields, and this enables us to capture the fracture process and the corresponding stress field based on theoretical considerations. In the dynamic tests, it is verified that multiple cracks appear simultaneously around the locations of maximum tensile stress and strain. Next, a matching approach based on theoretical models (i.e., the uniform and sinusoidal load models) is proposed to synchronize the stress and strain history curves in time, and the matching results show the tensile cracks are often generated prior to the peak stress as visualized in ultra-high-speed camera images. This peak stress corresponds to the failure of the sample structure, which is different from the material tensile strength as an inherent material property. In this study, we use the term "overloading" to describe the structural failure of the material. The difference between the peak stress and material tensile strength is associated with the time it takes for the crack to propagate, interact, and span the structure during the loading process, which is termed as "time-dependent structural failure". The strain-rate-dependent tensile strength of the alumina ceramics is computed with a correction method, and the tensile strength is defined as the tensile stress when the central crack first appears in the ultra-high-speed camera images. Then, the fracture surfaces of the alumina fragments are examined by Scanning electron microscopy to explore the fracture mechanism in the

*Corresponding author
Email address: jzheng11@ualberta.ca (Jie Zheng)

failure process. Finally, a strain-rate-dependent tensile strength model is proposed to describe the tensile strength of the CeramTec 98% alumina and other alumina ceramics in the literature.
Keywords: Strain-rate-dependent, Alumina ceramics, Flattened Brazilian disk, Tensile strength, split-Hopkinson pressure bar, Modelling

---

1. Introduction

Advanced ceramics are attractive for use in impact protection applications as a result of their low density, high hardness, and high wear resistance [1]. In the application of armour systems, ceramic materials are used as the first layer to blunt the projectile [2]. Upon impact, the ceramic materials crack and fail because, in part, of the reflected tensile waves generated from the back-free surface of the armour [3]. Thus, the wide application of advanced ceramics requires understanding the deformation and failure mechanisms that manifest under tensile loading. The challenges associated with performing conventional direct tensile tests on advanced ceramics have led to several indirect approaches (e.g., sleeve-fracturing tests, beam bending tests, and Brazilian tests) for assessing the tensile strength of ceramics [4, 5, 6]. Among these testing approaches, the Brazilian testing is suggested for studying the tensile strength of brittle materials for ease of manufacturing [7, 8, 9, 10, 11]. To reduce the stress concentration near the loading area, Wang et al. [12, 13, 14, 15] introduced two parallel flat ends on the Brazilian disk (termed the flattened Brazilian disk) of rock materials. In the dynamic Brazilian tests, Antonn et al. [16] found that the stress distribution was similar to the quasi-static one, and more dynamic Brazilian disk tests were carried out to investigate the strain-rate-dependent effect on the tensile strength of brittle materials [17, 18, 19, 20, 21, 22]. Recently, the flattened Brazilian disk and the split Hopkinson pressure bar (SHPB) are widely used in the literature to characterize the dynamic tensile strength of brittle materials [6, 15, 23, 24, 25, 26, 27]. In the dynamic Brazilian disk tests conducted by Mellor and Hawkes [28], the cracks appeared prior to the recorded peak load ("structural strength"), therefore, the tensile strength is likely overestimated without any correction [28]. This overestimation phenomenon is also mentioned in the Brazilian tests of concrete [29] and rock materials [30, 31]. However, little attention has been directed toward solving this problem. In the current study, experimental and theoretical methods are used to unravel the differences between the "structural strength" and the "material tensile strength" in Brazilian disk testing.

To obtain the stress and strain fields, the Brazilian disk test has also been extensively studied coupled with theoretical approaches [32, 33]. For example, Hondros [34] proposed a complete stress solution for the Brazilian disk under uniformly distributed loads, and he assumed the material was linearly elastic, homogeneous, and isotropic. Since then, several studies have investigated the exact solutions of the stress and strain fields to take anisotropy [35, 36] and

nonlinear deformation characteristics [37, 38] into account. In recent studies, Markides et al. [32, 39, 40] obtained the full-field solutions for stress and strain in the Brazilian disk under different types of loading distributions (e.g., the uniform and sinusoidal load), and he found that the stress and strain fields away from the disk's center were influenced by the different applied load. In addition to the mechanical properties, the other topic of interest in Brazilian disk testing is the problem of crack initiation and growth [31]. In some studies [38, 41], researchers hypothesized the central crack would occur first when the maximum tensile stress exceeded its tensile strength, based on the Griffith failure criterion. In other studies [31, 42], researchers thought the tensile cracks might initiate at the location where the tensile strain reached the critical extension strain. In the current study, we use insights from these theoretical studies [32, 39, 40] coupled with experimental methods to explore the fracture process of a CeramTec 98% alumina ceramic in the flattened Brazilian disk (FBD) test configuration.

Building on past works, the current study uses combined experimental and modelling methods to investigate the strain-rate-dependent tensile response of an alumina ceramic. Firstly, quasi-static and dynamic tests are carried out on a standard MTS machine and a modified split-Hopkinson pressure bar (SHPB) system. An ultra-high-speed camera coupled with digital image correlation (DIC) is used to measure the strain field. In Section 2.4, analytical solutions proposed by Markides et al. [32, 39, 40] are used to calculate the stress and strain of the Brazilian disk specimen along the vertical diameter based on the Saint-Venant principle [6, 13, 14, 15, 23, 24, 25, 26]. In the dynamic FBD tests, we find the splitting fracture of the FBD may not be controlled only by the Griffith failure criterion (the maximum tensile stress), but also by the maximum tensile strain. In Section 3.1, by using the proposed matching method in the current study, the "time-dependent structural failure" phenomenon is observed in the dynamic FBD tests of the alumina ceramic, thereby providing insights into the differences between "structural strength" and the "material tensile strength". Then, the strain-rate-dependent tensile strength of the CeramTec 98% alumina is achieved with a correction method that regards the stress when the central crack first appears as the tensile strength and is compared with other alumina ceramics under different loading rates. The fracture surfaces of the alumina fragments are examined using Scanning electron microscopy (SEM) to explore the failure mechanism in Section 3.2. Lastly, a strain-rate-dependent tensile strength model for alumina ceramics is proposed based on the one-dimensional elastic wave theory [43, 44, 45], the Griffith failure criterion

[31, 44, 46], and observations made in the current study and spall experiments [44, 47, 48]. Finally, in Section 3.3 and Section 3.4, this model is validated with the experimental results of the CeramTec 98% alumina and other alumina ceramics (i.e., A94, A98 and A99) [44, 46, 49, 50, 51].

2. Experimental and modelling methods

2.1. Material and specimens

In this study, a commercially available alumina ceramic ALOTEC 98 SB from CeramTec, Germany, is investigated, and it is referred to as CeramTec 98% in this paper. This ceramic has an alumina content of 98 mass percentage, a low porosity of less than 2%, high hardness of 13.5 GPa, a low density of 3.8 g/cm^3, Young's modulus of 335 GPa, and Poisson's ratio of 0.23. These mechanical properties are provided by the manufacturer [52] and evaluated in our previous studies [53, 54]. The FBD specimen has a diameter of 8 mm and thickness of 4 mm with two parallel flat ends corresponding to the loading angle $2\omega_0 = 20°$, as Figure 1 shows. The thickness to the diameter ratio is 0.5, which is recommended in the literature [9, 55]. The surfaces of the specimens were sprayed with speckle patterns to facilitate digital image correlation (DIC) analysis, and the methods are presented in detail later in this section.

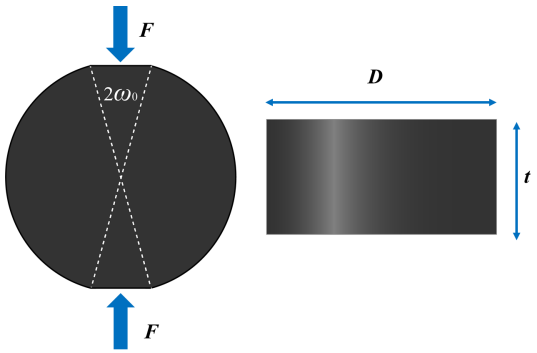

Figure 1: The schematic diagram of the FBD sample. The diameter D is 8 mm, thickness t is 4 mm, the loading angle $2\omega_0$ is 20°, and F is the applied loading in the test.

2.2. The flattened Brazilian disk tests

The quasi-static FBD tests were carried out using a MTS 810 materials testing machine with a ±100 kN load cell. The specimens were compressed under displacement control at a

loading speed in the range of $\sim 10^{-4}$ to $\sim 10^{-2}$ mm/s, and the loading direction of F is shown in Figure 1. A PROMON U750 high-speed camera with a full resolution of 1280 $\times$ 1024 pixel^2 was used to monitor the specimen surface during quasi-static testing. The acquisition rate of the camera was set between 5 and 500 frames per second (FPS), and its value is related to the loading speed. In FBD tests, shear failure might occur near the loading zone due to friction between loading platens and specimen [31, 40], as observed in many Brazilian disk tests of rocks [56]. To eliminate the frictional effects and prevent the premature edge failure (shear failure), high-pressure grease was applied between the surfaces of the loading platens and the flat ends of the specimen in both the quasi-static and dynamic FBD tests.

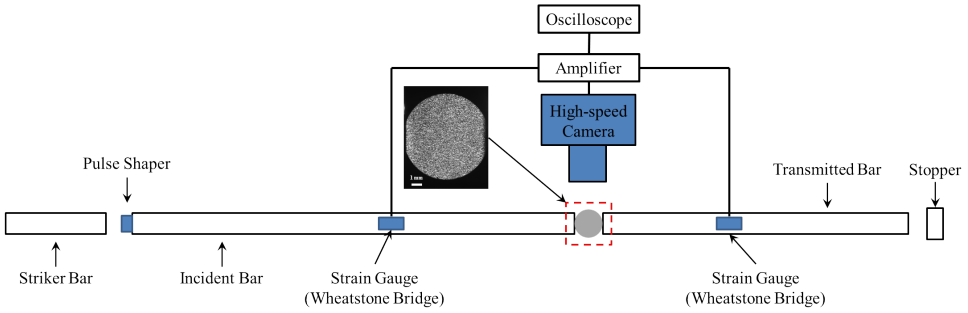

Figure 2: The split-Hopkinson pressure bar configuration for dynamic testing. This figure shows the schematics of the experimental setup and the typical camera view of an FBD sample.

Figure 2 shows the dynamic FBD test setup, and these were conducted using a 12.7mm diameter split-Hopkinson compression bar synchronized with an ultra-high-speed camera. The incident and transmitted bars were made from hardened C-350 maraging steel with an elastic modulus of 200 GPa and a density of 8080 kg/m^3, and they are 1016 mm and 914 mm in length, respectively. The experimental system used in this study was the same as in Koch et al. [57] and Lo et al. [58]. In addition, a long striker (304 mm in length) was chosen to provide a loading pulse recommended in literature [25, 59] to realize the dynamic force equilibrium and to maintain the equilibrium status until specimen failure. The pulse shapers (i.e., tin, high density polyethylene (HDPE), and paper) were also used in the dynamic test to control the rise time and profile of the incident pulse and achieve a constant strain rate [25, 53, 58]. In this study, the tin and HDPE pulse shapers are 1.59 mm in thickness and 3.97 mm in diameter, and the paper pulse shaper is 0.1 mm in thickness and 3.97 mm in diameter. During the dynamic tests, the

images were recorded by a Shimadzu HPV X-2 ultra-high-speed camera with a SIGMA F2.8EX DG MACRO OS lens with a full resolution of 400 × 250 pixel^2 and a focal length of 105 mm. To monitor the specimen surface with different strain rates, the exposure time was chosen in the range of 200 to 500 ns, and the framing rate was selected in the range of 0.5 to 2 million fps.

Two strain gauges (Micro 184 Measurements CEA-13–250UN-350) on the incident and transmission bars were used to measure the incoming, reflected, and transmitted pulses. An HBM Gen3i High-Speed Recorder was employed for the data acquisition from the strain gauges at 4 MHz with a Bessel IIR pre-filter to eliminate low-frequency noise. For the theory of the SHPB system, the stress wave propagation analysis has been well documented by Song and Chen [45]. Using the strain gauge signal, the dynamic loading applied to the specimen was computed from the classical one-dimensional wave propagation theory [60, 61], as we will now explain.

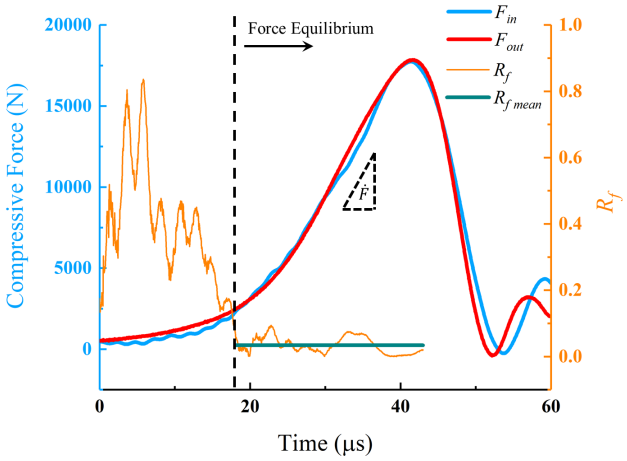

Figure 3: The check for force equilibrium in the dynamic FBD test. The F_{in} is the incident bar force obtained from the incident and reflected signals. The F_{out} is the transmitted bar force obtained from the transmitted signal. R_f is a factor related to the force equilibrium. R_{fmean} is the mean value of R_f during the loading process in the dynamic FBD test when the force equilibrium is achieved. Finally, the $\dot{F}$ is the loading rate obtained from the slope of the loading curve.

In all the dynamic tests of the current study, force equilibrium was achieved. For example, Figure 3 shows a representative force equilibrium plot comparing the force applied to the specimen surface in contact with the incident bar F_{in} (obtained from the incident and reflected

signals) and the force on the specimen surface in contact with the transmitted bar F_{out} (obtained directly from the transmitted signal). A factor R_f is used to evaluate the relative difference between F_{in} and F_{out} [6, 25, 62]:

$$R_f = 2\left|\frac{F_{in} - F_{out}}{F_{in} + F_{out}}\right| \tag{1}$$

In Figure 3, R_f has a higher value at the beginning and then drops dramatically with an average value of $R_{fmean} = 0.034$ starting around 18 μs during the loading process in the dynamic FBD test. The evolution of R_f in the current study is similar to the observations in the experimental studies of Khosravani et al. [25] and Zhang et al. [6, 63]. As a result, our experimental results satisfy the criterion for force equilibrium in brittle materials (less than 5%) [6, 25, 64] during the loading process in the dynamic FBD tests. Thus, a good force equilibrium was achieved during the loading process in the dynamic FBD test at around 18 μs. Due to the linear increase of the loading force, a constant loading rate $\dot{F} = 8.69\times10^8$ N/s can be determined by the slope of the force-time curve in Figure 3.

Finally, the engineering strain was obtained from DIC analysis. In the current study, a commercial software, VIC2D V6 (Irmo, South Carolina, USA), was used for the DIC analysis in both quasi-static and dynamic experiments. During analysis, according to the different loading rates, the area of interest was discretized into a subset size between 23 × 23 and 31 × 31 pixel^2 and step sizes between 3 and 5 pixels to minimize the correlation error, as recommended in literature [2, 6, 51, 65]. The zero-normalized sum of squared differences (ZNSSD) criterion with the optimized eight-tap interpolation scheme was utilized in the analysis. Pre-filtering of images was done with a low-pass filter, and subset weighting was done via a Gaussian weighting, as recommended in literature [58, 66].

2.3. Post-mortem fractographic analysis

The microstructure of the as-received CeramTec 98% alumina had been investigated in our previous study [53] by Scanning electron microscopy (SEM), Electron Backscatter Diffraction (EBSD), energy-dispersive x-ray spectroscopy (EDS), and X-Ray Microscopy (XRM) methods. In this study, post-mortem fracture surfaces of tested samples were studied by SEM analysis. This analysis was carried out using a Zeiss Sigma machine (Oberkochen, Baden-Württemberg, Germany). The micrographs were obtained using an In-Lens (IL) detector. The machine was operated with the electron high tension voltage at 10 kV and a working distance of ∼5 mm.

2.4. Theoretical considerations

In addition to obtaining the strain field by DIC analysis, the current study uses a theoretical approach to estimate and explore the stress and strain fields during FBD testing. The stress and strain used in the current study are the nominal stress and engineering strain because the failure deformation of the alumina ceramic is small (i.e., failure strain < 0.003). There is no direct analytical solution of the stress and strain fields for the FBD geometry, but the equivalent method based on the Saint-Venant principle can give an approximate analytical solution of the stress and strain fields near the disk's center [12, 13, 14]. For example, based on the equivalent uniformly distributed load in Figure 4, the tensile strength, σ_t, at the center of the FBD sample is given by Wang et al. [14]:

$$\sigma_t = k\frac{2F}{\pi Dt} \tag{2}$$

where σ_t is the tensile strength in the radial direction (xx), D and t are the diameter and thickness of the sample, and k is a non-dimensional factor depending on the loading angle whose value is 0.9644 when $2\omega_0 = 20°$. In the literature, this equivalent uniformly distributed load method was used to give an approximate solution for the FBD tests in both quasi-static [12, 13, 14] and dynamic [6, 15, 23, 24, 25, 26] conditions.

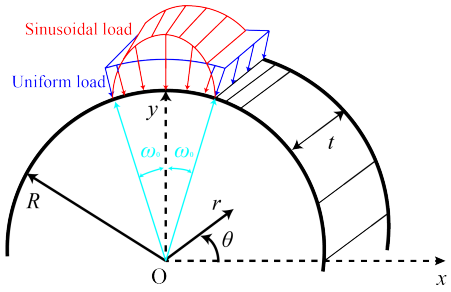

Figure 4: Schematic representation of two kinds of loading types exerted on the disk, and these equivalent methods can provide an approximate analytical solution for the FBD tests [14]. The blue load is the equivalent uniformly distributed load and the red load is the equivalent sinusoidal distributed load. The $2\omega_0$ is the loading angle, and its value is the same as that in an FBD with $2\omega_0 = 20°$. R and t are the radius and thickness of the sample, respectively, and their values are the same as the FBD. (r, θ) is an arbitrary point on the sample in polar coordinates.

In the literature, researchers have also been interested in the stress and strain distribution along the vertical diameter (denoted as y-axis in Figure 4) [31, 33, 67], which is parallel to

the loading direction. These stress and strain fields away from the disk's center are influenced by the exact distribution of the applied load [40, 67], which may affect tensile crack initiation [31]. To investigate the influence of the load distribution, both uniform and non-uniform (i.e., sinusoidal) distributed loads are selected in the current study to predict the stress and strain along the vertical diameter, as Figure 4 shows schematically.

For the equivalent uniformly distributed load in Figure 4, the stress along the vertical diameter is given by Markides et al. [32]:

$$\begin{aligned}\sigma_{rr}=&\frac{p}{\pi}\left[2\omega_0+\arctan\left(\frac{R\cos\omega_0-r\sin\theta}{R\sin\omega_0-r\cos\theta}\right)+\arctan\left(\frac{R\cos\omega_0+r\sin\theta}{R\sin\omega_0+r\cos\theta}\right)+\right.\\&\arctan\left(\frac{R\cos\omega_0-r\sin\theta}{R\sin\omega_0+r\cos\theta}\right)+\arctan\left(\frac{R\cos\omega_0+r\sin\theta}{R\sin\omega_0-r\cos\theta}\right)-2\pi-\\&\left.R^2(R^2-r^2)\left(\frac{\sin 2(\theta-\omega_0)}{R^4+2(rR)^2\cos 2(\theta-\omega_0)+r^4}-\frac{\sin 2(\theta+\omega_0)}{R^4+2(rR)^2\cos 2(\theta+\omega_0)+r^4}\right)\right]\end{aligned} \tag{3}$$

$$\begin{aligned}\sigma_{\theta\theta}=&\frac{p}{\pi}\left[2\omega_0+\arctan\left(\frac{R\cos\omega_0-r\sin\theta}{R\sin\omega_0-r\cos\theta}\right)+\arctan\left(\frac{R\cos\omega_0+r\sin\theta}{R\sin\omega_0+r\cos\theta}\right)+\right.\\&\arctan\left(\frac{R\cos\omega_0-r\sin\theta}{R\sin\omega_0+r\cos\theta}\right)+\arctan\left(\frac{R\cos\omega_0+r\sin\theta}{R\sin\omega_0-r\cos\theta}\right)-2\pi+\\&\left.R^2(R^2-r^2)\left(\frac{\sin 2(\theta-\omega_0)}{R^4+2(rR)^2\cos 2(\theta-\omega_0)+r^4}-\frac{\sin 2(\theta+\omega_0)}{R^4+2(rR)^2\cos 2(\theta+\omega_0)+r^4}\right)\right]\end{aligned} \tag{4}$$

with

$$p=\frac{F}{2Rt\sin\omega_0} \tag{5}$$

where F is the total force applied to the specimen, $\theta = 90°$, and r is in the range of 0 to 4 mm as we are interested in the values from the center to the outer edge of the disk. σ_{rr} and $\sigma_{\theta\theta}$ are two normal stress in polar coordinates, and they can be transformed into the Cartesian coordinates: $\sigma_{yy} = \sigma_{rr}$ and $\sigma_{xx} = \sigma_{\theta\theta}$ with $x = 0$ and y in the range of 0 to 4 mm. The ω_0 is the loading angle, and its value is the same as the one in FBD $2\omega_0 = 20°$. R and t are the radius and thickness of the sample, respectively, which are both 4 mm.

Next, in one study of dynamic FBD tests, Wang et al. [15] found the stress distribution is non-uniform at the two flat ends of the specimen. The sinusoidal load model considered the

contact and deformation between the specimen and loading device by assuming a non-uniform distribution of radial pressure [39]. Although, it is generally accepted that the different types of load distributions would not seriously influence the stress or strain field at the center of the Brazilian disk [14, 40], but this condition is not appropriate for the area far away from the center along the vertical diameter in Figure 4 [40]. In the current study, we investigate the influence of the loading distribution on the stress and strain field along the vertical diameter ($x = 0$ and y in the range of 0 to 4 mm for the equivalent sample in Figure 4). For the equivalent sinusoidal distributed load, the stress along the vertical diameter is given by Markides et al. [39]:

$$
\begin{aligned}
\sigma_{rr}=&\frac{c}{2\pi}\left\{-4\omega_0\cos\omega_0+\frac{\left(R^2-r^2\right)^2}{2Rr^3}\cdot\right.\\
&\cos\theta\left(\ln\sqrt{\frac{R^2+r^2-2Rr\sin(\theta-\omega_0)}{R^2+r^2-2Rr\sin(\theta+\omega_0)}}-\ln\sqrt{\frac{R^2+r^2+2Rr\sin(\theta-\omega_0)}{R^2+r^2+2Rr\sin(\theta+\omega_0)}}\right)+\\
&\left(\frac{r^4+4R^2r^2-R^4}{2Rr^3}\sin\theta-2\cos\omega_0\right)\left(\arg(t_1-z)-\arg(t_2-z)\right)-\\
&\left(\frac{r^4+4R^2r^2-R^4}{2Rr^3}\sin\theta+2\cos\omega_0\right)\left(\arg(t_1+z)-\arg(t_2+z)\right)+\frac{R^2-r^2}{r}\cdot\\
&\left[\left(\frac{r^2\cos2\theta-R^2}{2Rr}+\cos\omega_0\sin\theta\right)\left(\frac{R\sin\omega_0-r\cos\theta}{R^2+r^2-2Rr\sin(\theta+\omega_0)}+\frac{R\sin\omega_0+r\cos\theta}{R^2+r^2-2Rr\sin(\theta-\omega_0)}\right)-\right.\\
&\left(\frac{r\sin2\theta}{2R}-\cos\omega_0\cos\theta\right)\left(\frac{-R\cos\omega_0+r\sin\theta}{R^2+r^2-2Rr\sin(\theta+\omega_0)}+\frac{R\cos\omega_0-r\sin\theta}{R^2+r^2-2Rr\sin(\theta-\omega_0)}\right)+\\
&\left(\frac{r^2\cos2\theta-R^2}{2Rr}-\cos\omega_0\sin\theta\right)\left(\frac{R\sin\omega_0+r\cos\theta}{R^2+r^2+2Rr\sin(\theta+\omega_0)}+\frac{R\sin\omega_0-r\cos\theta}{R^2+r^2+2Rr\sin(\theta-\omega_0)}\right)-\\
&\left.\left.\left(\frac{r\sin2\theta}{2R}+\cos\omega_0\cos\theta\right)\left(\frac{-R\cos\omega_0-r\sin\theta}{R^2+r^2+2Rr\sin(\theta+\omega_0)}+\frac{R\cos\omega_0+r\sin\theta}{R^2+r^2+2Rr\sin(\theta-\omega_0)}\right)\right]\right\}
\end{aligned}
\tag{6}
$$

$$\sigma_{\theta\theta}=\frac{c}{2\pi}\left\{-4\omega_0\cos\omega_0+\frac{3r^4-2R^2r^2-R^4}{2Rr^3}\cdot\right.$$
$$\cos\theta\left(\ln\sqrt{\frac{R^2+r^2-2Rr\sin(\theta-\omega_0)}{R^2+r^2-2Rr\sin(\theta+\omega_0)}}-\ln\sqrt{\frac{R^2+r^2+2Rr\sin(\theta-\omega_0)}{R^2+r^2+2Rr\sin(\theta+\omega_0)}}\right)+$$
$$\left(\frac{3r^4+R^4}{2Rr^3}\sin\theta-2\cos\omega_0\right)(\arg(t_1-z)-\arg(t_2-z))-$$
$$\left(\frac{3r^4+R^4}{2Rr^3}\sin\theta+2\cos\omega_0\right)(\arg(t_1+z)-\arg(t_2+z))-\frac{R^2-r^2}{r}\cdot$$
$$\left[\left(\frac{r^2\cos2\theta-R^2}{2Rr}+\cos\omega_0\sin\theta\right)\left(\frac{R\sin\omega_0-r\cos\theta}{R^2+r^2-2Rr\sin(\theta+\omega_0)}+\frac{R\sin\omega_0+r\cos\theta}{R^2+r^2-2Rr\sin(\theta-\omega_0)}\right)-\right.$$
$$\left(\frac{r\sin2\theta}{2R}-\cos\omega_0\cos\theta\right)\left(\frac{-R\cos\omega_0+r\sin\theta}{R^2+r^2-2Rr\sin(\theta+\omega_0)}+\frac{R\cos\omega_0-r\sin\theta}{R^2+r^2-2Rr\sin(\theta-\omega_0)}\right)+$$
$$\left(\frac{r^2\cos2\theta-R^2}{2Rr}-\cos\omega_0\sin\theta\right)\left(\frac{R\sin\omega_0+r\cos\theta}{R^2+r^2+2Rr\sin(\theta+\omega_0)}+\frac{R\sin\omega_0-r\cos\theta}{R^2+r^2+2Rr\sin(\theta-\omega_0)}\right)-$$
$$\left.\left.\left(\frac{r\sin2\theta}{2R}+\cos\omega_0\cos\theta\right)\left(\frac{-R\cos\omega_0-r\sin\theta}{R^2+r^2+2Rr\sin(\theta+\omega_0)}+\frac{R\cos\omega_0+r\sin\theta}{R^2+r^2+2Rr\sin(\theta-\omega_0)}\right)\right]\right\} \tag{7}$$

with

$$\begin{aligned}
c&=\frac{F}{2Rt(\sin\omega_0-\omega_0\cos\omega_0)};\\
\arg(t_1-z)&=\arctan\left(\frac{R\cos\omega_0-r\sin\theta}{R\sin\omega_0-r\cos\theta}\right);\\
\arg(t_1+z)&=\pi+\arctan\left(\frac{R\cos\omega_0+r\sin\theta}{R\sin\omega_0+r\cos\theta}\right);\\
\arg(t_2-z)&=\pi-\arctan\left(\frac{R\cos\omega_0-r\sin\theta}{R\sin\omega_0+r\cos\theta}\right);\\
\arg(t_2+z)&=\pi-\arctan\left(\frac{R\cos\omega_0+r\sin\theta}{R\sin\omega_0-r\cos\theta}\right).
\end{aligned} \tag{8}$$

Our study only focuses on the vertical diameter (or y-axis) in Figure 4, thus $\theta = 90°$ (or x=0) and r (or y) is in the range of 0 to 4 mm. In the later part of this paper, the Cartesian coordinates are used to describe the stress and strain fields, thus $\sigma_{xx} = \sigma_{\theta\theta}$ and $\sigma_{yy} = \sigma_{rr}$ in Equations (3), (4), (6) and (7) with $y = r$ (in the range of 0 to 4 mm) and $x = 0$ (corresponding to $\theta = 90°$).

Figure 5 shows the stress distribution along the vertical diameter (denoted as y-axis in Figure 4) under a total compressive force $F = 5.25$ kN using the above-mentioned models. It should be noted that when the force equilibrium is realized in the experiment, the stress and strain distribution in the dynamic test is considered the same as the quasi-static [15, 64, 68]. Thus, based on the force equilibrium in Figure 3, the total compressive force $F = 5.25$ kN is selected for both quasi-static and dynamic tests. Figure 5 shows that the uniform and sinusoidal load models compute the same tensile stress at the disk's center ($x = 0$ and $y = 0$), but differences appear when the location is away from the center (around $x = 0$ and $y > 2.5$ mm). The maximum tensile stress σ_{xx} appears at the disk's center, and the tensile stress decreases slightly within 3 mm but drops dramatically when y is larger than 3 mm. This result is consistent with the conclusion made by Markides et al. [39] that the stress field around the center region ($x = 0$ and $y < 2.5$ mm in the current study) is insensitive to the exact loading application mode, but the critical differences appear near the loading vicinity ($x = 0$ and $y > 2.5$ mm in the current study).

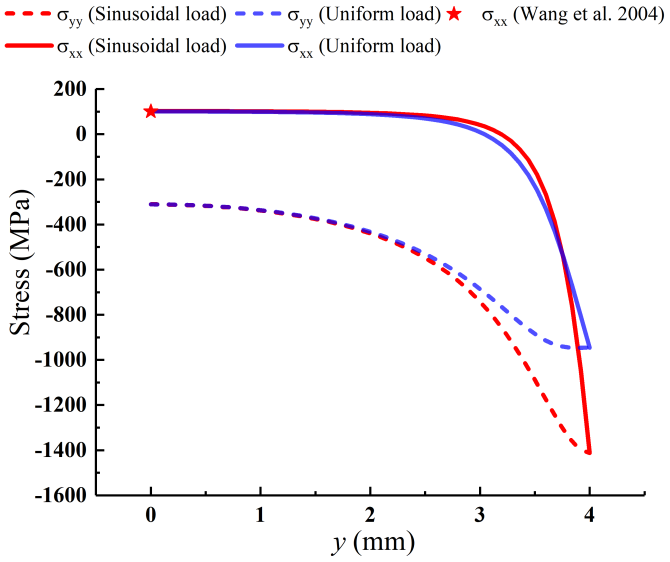

Figure 5: The stress distribution along the vertical diameter under a total compressive force of $F = 5.25$ kN obtained by different models. The σ_{yy} and σ_{xx} curves under uniform load are obtained by Equations (3) and (4) [32], and the σ_{yy} and σ_{xx} curves assuming a sinusoidal load are obtained by Equations (6) and (7) [39]. The point of σ_{xx} is obtained by Equation (2) [12, 13, 14].

2.5. The strain-rate-dependent tensile strength model

In this section, we reveal the relationship between strain rate and tensile strength for alumina ceramics based on one-dimensional elastic wave theory [43, 44, 45]. The model proposed here is also based on the post-mortem fractographic analysis made in the current study (discussed in Section 3.4) that failure processes of alumina is governed by the intergranular and transgranular micro-cracks, and the experimental observations of spall tests [44, 47, 48] that the failure process of alumina ceramics began with a single initial crack when encountered by the first reflected tensile pulse, although other secondary cracks appearred subsequently by the later reflected pulse. Thus, the dynamic tensile strength of alumina ceramics is dominated by the defects that generate the single primary initial crack. The experimental results presented in Gálvez et al. [46] and Dıaz-Rubio et al. [44] followed the Griffith failure criterion that the specimen failed at the point where the tensile stress exceeded the material tensile strength [31]. From this and considering a square tensile incident pulse passing through a potential cracking section with defects (e.g., micro-crack), the reflected and transmitted waves would be generated due to discontinuity, according to:

$$\begin{aligned} \sigma^{in} &= -\rho \cdot c \cdot v^{in} \\ \sigma^{-} &= \rho \cdot c \cdot v^{-} \\ \sigma^{+} &= -\rho \cdot c \cdot v^{+} \end{aligned} \tag{9}$$

where $\sigma^{in}, v^{in}, \sigma^{-}, v^{-}, \sigma^{+}$ and v^{+} are the stresses and particle velocities of incident, reflected and transmitted waves at the interface of the potential cracking section inside the sample, respectively. An equilibrium is achieved at the two sides of the flaw prior to failure when:

$$\sigma^{+} = \sigma^{in} + \sigma^{-} \tag{10}$$

Also, we assume that the strength of the flaw decreases due to the opening of the flaw, and this assumption is based on the linear degradation law [69]:

$$\sigma^{+} = \sigma_{cr}(1 - \frac{\delta}{\delta_{cr}}) \tag{11}$$

where σ_{cr} is the critical stress leading the material to degrade. Later in the strain-rate-dependent tensile strength model (Equation (18)), we would find the value of σ_{cr} equals the quasi-static tensile strength, which is determined experimentally. δ_{cr} is the critical micro-crack opening

displacement, and the material fails when $\delta = \delta_{cr}$. Finally, we have the relationship linking the crack opening displacements and particle velocities at the interface of the potential cracking section inside of the sample [43, 44, 45]:

$$\dot{\delta} = v^{+} - (v^{in} + v^{-}) \tag{12}$$

Combining Equations (9) to (12), we define::

$$\dot{\sigma}^{+} = \frac{2\sigma_{cr}}{\rho \cdot c \cdot \delta_{cr}}(\sigma^{+} - \sigma^{in}) \tag{13}$$

whose solution to the ordinary differential Equation (13) is:

$$\sigma^{+} = \sigma^{in} + (\sigma_{cr} - \sigma^{in}) \cdot e^{\frac{t}{t_c}} \tag{14}$$

where t_c is a constant value related to the material properties:

$$t_c = \frac{\rho \cdot c \cdot \delta_{cr}}{2\sigma_{cr}} \tag{15}$$

From this, we determine that failure results in $\sigma^{+} = 0$ and $\delta = \delta_{cr}$ at a time $t = \tau$, where τ is defined as the time to fail. Equation (14) becomes:

$$\sigma_0 = \sigma^{in} = \sigma_{cr} \cdot \frac{e^{\tau/t_c}}{e^{\tau/t_c} - 1} \tag{16}$$

where σ_0 is the tensile strength associated with failure from the initial flaw.

The time τ is the failure time of a square pulse. In this study, the loading force is a triangle pulse with a constant strain rate $\dot{\varepsilon}$. The empirical transformation that converts the strain rate of a triangle pulse ($\dot{\varepsilon}$) to the equivalent failure time of a square pulse (τ) is given by the linear regression method [70]:

$$\frac{\tau}{t_c} = a \cdot \dot{\varepsilon}^{-0.5} \tag{17}$$

Here, a is a constant factor associated with the strain rate sensitivity (discussed in Section 3.4), and its value can be obtained by curve fitting with the experimental results.

Finally, by combining Equations (16) and (17), we define a relationship describing the strain-rate-dependent tensile strength of alumina ceramics:

$$\sigma_0 = \sigma_{cr} \cdot \frac{e^{a \cdot \dot{\varepsilon}^{-0.5}}}{e^{a \cdot \dot{\varepsilon}^{-0.5}} - 1} \tag{18}$$

As a limiting case for quasi-static conditions, $\dot{\varepsilon}$ is a extremely small value and the quasi-static tensile strength is $\sigma_0 = \sigma_{cr}$ based on Equation (18). In Section 3.4, we apply this strain-rate-dependent tensile strength model (Equation (18)) to the experimental results from this study and the literature [44, 46, 49, 50].

3. Results and discussion

Figure 6 shows typical experimentally measured tensile stress and strain history curves for the disk's center in a dynamic test. The stress history curve at the disk's center is obtained from the force curve in Figure 3, as well as using the models proposed in Equations (4) and (7) assuming both a uniform and sinusoidal distributed load. These two models (Equations (4) and (7)) can obtain the same stress history curve at the disk's center, which is mentioned in Figure 5. The strain history in Figure 6 is obtained experimentally by DIC, where a rapid increase in strain is observed at around 70 μs. This rapid increasing turning point corresponds to the onset of a crack at the center of the disk in the dynamic FBD test (more details are discussed in Section 3.2). Some studies [25, 28] have noted that correlating the peak stress and the onset of the center crack (i.e., the turning point in Figure 6) may lead to overestimation of tensile strength. The current study proposes a new matching method to solve the overestimation problem and determine the tensile strength as the stress when the central crack first occurs.

3.1. The temporally- and spatially-evolving strain components

In these experiments, the loading history $F(t_1)$ is obtained from the SHPB or MTS system with the recorded time t_1, and the DIC system can measure the strain history $\varepsilon(t_2)$ at the disk's center with a different recorded time t_2. The matching method proposed here is to determine the delay time t_0 between the recorded time t_1 and t_2 from the two different systems. In the current study, we use the strain history of the disk's center to carry out the matching. The theoretical results of the uniform and sinusoidal loading models are the same for the disk's center; thus, we can choose either the uniform or sinusoidal loading model (Equations (4) and (7)) to calculate the predicted results at the disk's center. The method is described as follows:

1. Based on the experimental method, the loading history $F(t_1)$ is obtained from the SHPB or MTS system with the recorded time t_1, and the DIC system can measure the strain history $\varepsilon(t_2)$ with a different recorded time t_2;

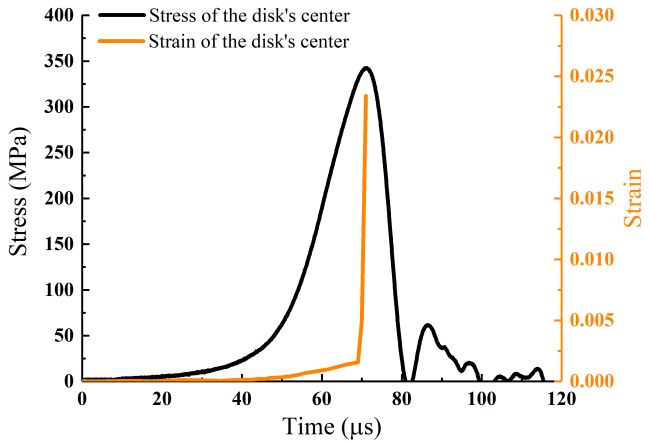

Figure 6: An example of the tensile stress (σ_{xx}) and strain (ε_{xx}) history of the disk's center ($x = 0$ and $y = 0$ mm) in a dynamic test. Here, the stress and strain curves are in different system times, the SHPB or MTS system time and the DIC system time, respectively.

2. Next, the theoretical stress history curve $\sigma(t_1)$ for the disk's center can be obtained by the loading history $F(t_1)$ and assuming a uniform or sinusoidal loading model;

3. Then, the theoretical strain history curve $\varepsilon(t_1)$ can be estimated by adopting Hooke's law generalized for isotropic linear-elastic materials;

4. Then, the theoretical results $\varepsilon(t_1)$ can be matched with the DIC strain history curve $\varepsilon(t_2)$ in time to find out the delay time t_0.

5. Lastly, the $\varepsilon(t_1 - t_0)$, $\sigma(t_1 - t_0)$ and $F(t_1 - t_0)$ obtained from the SHPB or MTS system are matched with $\varepsilon(t_2)$ obtained from the DIC system.

Based on the matching method, Figure 7 compares the theoretically calculated strain components with experimental results for the disk's center during the loading period in the dynamic FBD test with a loading rate of $\dot{F} = 8.69{\times}10^8$ N/s. From Figure 7, it is observed that the experimental results are consistent with the theoretical predictions, with the main difference appearing around 70 μs, where the DIC strain component increases (for ε_{xx}) or decreases (for ε_{yy}) rapidly prior to the peak predicted strain and stress. This is due to the fast expansion from cracking at the disk's center that occurs at around 70 μs (more details about the cracking are

discussed in Section 3.2). The discrepancies between the theoretical and experimental strains are relatively small before 70 μs, and the material behaves linear-elastically. As an outcome of the linearly increasing part in the tensile strain curve, a constant tensile strain rate of $\dot{\varepsilon} = 91$ s^{-1} can be determined by the slope of the ε_{xx} history curve in Figure 7a. In the current study, all the tensile strain rates ($\dot{\varepsilon}$) are calculated for the disk center ($x = 0$ and $y = 0$), and their values are obtained from the slope of the ε_{xx} history curve.

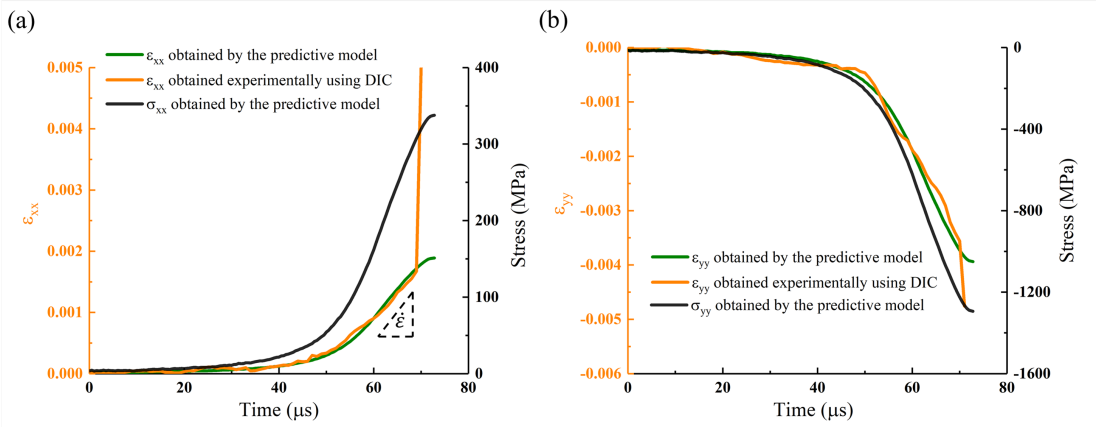

Figure 7: The DIC strain vs. predicted strain for the disk's center ($x = 0$ and $y = 0$) of the FBD sample in a dynamic test with a loading rate of $\dot{F} = 8.69\times10^8$ N/s. The predicted strain is obtained by Equations (4) and (7) and Hooke's law. The DIC strain history $\varepsilon_{xx}(t_2)$ in (a) is the same as that in Figure 6, and here we only show some part of it for the value of $\varepsilon_{xx}(t_2)$ within 0.005. The $\dot{\varepsilon}$ is the tensile strain rate calculated from the slope of $\varepsilon_{xx}(t_1 - t_0)$ obtained by the theoretical model. The stress history curves are also shown in the figures, and the stress history $\sigma(t_1 - t_0)$ is matched with the DIC strain history $\varepsilon_{xx}(t_2)$ in time.

In addition to investigating the *temporally-evolving* strain components shown in Figure 7, the current study also investigates the *spatially-evolving* strain components along the vertical diameter (the y-axis with $x = 0$ mm) under a total compressive force of $F = 5.25$ kN, as Figure 8a and b show for ε_{xx} and Figure 8 c and d show for ε_{yy}. The force $F = 5.25$ kN is selected because force equilibrium is achieved under this condition, as Figure 3 shows. When the force equilibrium is achieved, the stress and strain distribution in the dynamic test is considered the same as in the quasi-static test [15, 64, 68].

First, Figure 8a shows the distribution of ε_{xx} along the vertical diameter (the y-axis with $x = 0$ mm) under a total compressive force of $F = 5.25$ kN, where the blue and red curves

are obtained by assuming the uniform and sinusoidal loading models. For the two curves of ε_{xx}, it can be seen that the tensile strain will increase slightly along y from the center to the loading area and then drop dramatically. Specifically, the two curves of ε_{xx} are almost the same within $y = 2.5$ mm, but the difference becomes larger when y is greater than 2.5 mm, as the inset in Figure 8a shows. In addition, experimental results from quasi-static (Qs) and dynamic (Dyn) testing are plotted in Figure 8a, and the following number in the legend is the loading rate obtained from the slope of the loading curve (shown in Figure 3). Although the maximum tensile stress is located at the disk's center ($x = 0, y = 0$ mm) as Figure 5 shows, the maximum tensile strain occurs away from the disk's center as Figure 8a shows. In the uniform loading model, the maximum tensile strain appears at approximately $x = 0, y = 2.5$ mm, which is approximately 13% greater than the value at the disk's center. Similarly, in the sinusoidal loading model, the location of the maximum tensile strain is around $x = 0, y = 2.8$ mm, and its value is around 27% greater than the tensile strain at the disk's center. Averaging across all the experimental results, the maximum tensile strain is located between y =2 and 3.2 mm with $x = 0$ mm, and its value is around 17% to 40% greater than the tensile strain at the disk's center. To better demonstrate the location of the maximum tensile strains, Figure 8b shows the full tensile strain (ε_{xx}) field of a sample under a total compressive force of $F = 5.25$ kN in the "Qs 7.55×10^2N/s" test. It is observed that a band with large tensile strain appears along the y-axis, with the maximum tensile strain being 0.00073 at around $x = 0, y = 2.9$ mm when compared with 0.00053 at the disk center. This observation justifies the model prediction. The strain component ε_{yy} along the vertical diameter is also shown in Figure 8c. Similarly, the two curves of ε_{yy} obtained from the two models are almost the same within $y = 2.5$ mm, but the difference becomes larger when y is higher than 2.5 mm. According to the experimental results, ε_{yy} decreases faster than the results of the predictive models. In addition, the full strain (ε_{yy}) field of the sample in the "Qs 7.55×10^2N/s" test is shown in Figure 8 d. It is observed that the maximum compressive strain is near the loading vicinity ($x = 0$ and $y > 3$ mm), which justifies the model prediction.

Overall, by comparing the predictive curves obtained by the two models with the experimental results in Figure 8, we find that both the uniform and sinusoidal loading models are consistent with the experimental results within $y < 2.5$ mm. However, the differences become large when $y > 2.5$ mm. The discrepancies between the theoretical and experimental results

may come from: 1) the real load distribution is complicated and different from the uniform and sinusoidal load distribution [12, 13, 14]; 2) the material microstructure is not homogeneous and the defects inside the material may have significant effects on stress and strain distributions [31]. In this paper, the main purpose of comparing the results of two models and experiments is to show that the loading distribution would affect both the values and locations of the maximum tensile strain along the vertical diameter, but has almost no influence on the area near the disk's center where the maximum tensile stress exists.

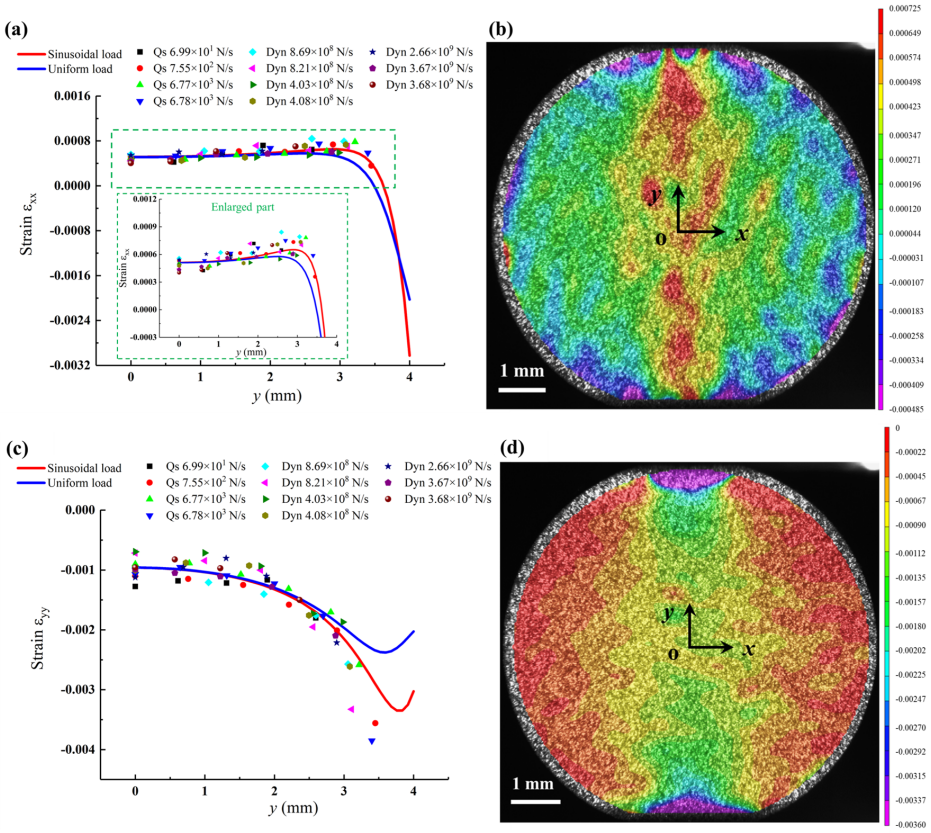

Figure 8: This figure shows ε_{xx} and ε_{yy} distributions under a total compressive force of $F = 5.25$ kN. a) The blue and red curves are the ε_{xx} distribution along the vertical diameter ($x = 0$ and $y = 0$ to 4 mm) obtained from the uniform (Equation (4)) and sinusoidal (Equation (7)) loading models. The points in the figure are obtained from experimental results with different loading rates. b) The ε_{xx} field of the sample surface obtained from the "Qs 7.55×10^2N/s" test. c) This figure includes the ε_{yy} distribution along the vertical diameter ($x = 0$ and $y = 0$ to 4 mm) obtained from the uniform Equation (3) and sinusoidal Equation (6) loading models, and the points are obtained from experiments with different loading rates. d) The ε_{yy} field of the sample surface in the "Qs 7.55×10^2N/s" test.

The phenomenon that the locations of maximum tensile stress and maximum tensile strain are different along the compressive diametral line has also been observed in Brazilian disk tests involving polymethylmethacrylate (PMMA) material [40] and rock materials [31, 56]. This phenomenon occurs because the material is in a local biaxial stress state along the vertical diameter, which is the main disadvantage of using BD tests to calculate the tensile strength [71]. The different locations of the maximum stress and strain and their linkages to the crack

initiation location in the BD test has been a topic of interest in the literature [31, 38, 41]. In some studies [38, 41], researchers thought the central crack would occur first when the maximum tensile stress exceeds its tensile strength based on the Griffith failure criterion. For example, in one study involving the dynamic FBD tests of rock material, Wang et al. [15] had found the location of crack initiation is the center of the FBD sample with a loading angle $2\omega_0$=20° (the same as the current study) by using strain gauges. However, in other studies [31, 42], researchers postulated that the tensile cracks might initiate at the location where the tensile strain reaches the critical extension strain. To investigate the crack initiation location of the alumina ceramic, in the current study, an ultra-high-speed camera is used to monitor the surface cracks in the dynamic FBD tests. Based on this, in the following section, we will unravel the relationship between the loading distribution, maximum tensile stress, maximum tensile strain, and crack initiation in the dynamic tests.

3.2. The fracture process of the FBD sample in a dynamic test

Here, we explore the fracture process of the FBD sample in the dynamic test. The reason why we do not show the fracture process of the quasi-static tests is that our quasi-static camera is not fast enough to capture the process. An appropriate speed camera could be triggered manually to capture the quasi-static fracture process, such as in Swab et al. [72]. However, we were unsuccessful in using our ultra-high-speed camera in capturing meaningful data in the quasi-static experiments. The fracture processes happen in μs [72, 73], which is extremely short compared with the loading time (e.g., seconds) in the quasi-static tests; therefore, triggering is challenging. While this is the case, we do note that the fracture processes have almost no influence on the strain and stress history in quasi-static conditions, which will be fully discussed in Section 3.3. Included in Figure 9 are time-resolved images showing the fracture process of a disk and the associated DIC contours with a loading rate of $\dot{F} = 8.69\times10^8$ N/s imaging at 1M fps. At 69 μs, no crack is observed on the sample surface in Figure 9a and d. However, in Figure 9b and e, four cracks appear simultaneously at 70 μs at around $x = 0$, $y = 0$ mm and $x = 0$, $y = \pm2.5$ mm; these are pointed out by the yellow arrows in Figure 9e. The locations of maximum tensile stress is around $x = 0$ and $y = 0$ mm and maximum tensile strain is around $x = 0$ and $y = 2.5$ mm in the "Dyn 8.69×10^8 N/s" test, shown in Figure 5 and Figure 8a. In all the dynamic tests, it is observed that multiple cracks appear simultaneously around the

locations of maximum tensile stress and strain. This observation suggests that the splitting fracture of a Brazilian disk may not be controlled only by the Griffith failure criterion (the maximum tensile stress), but also by the maximum tensile strain in dynamic tests [31].

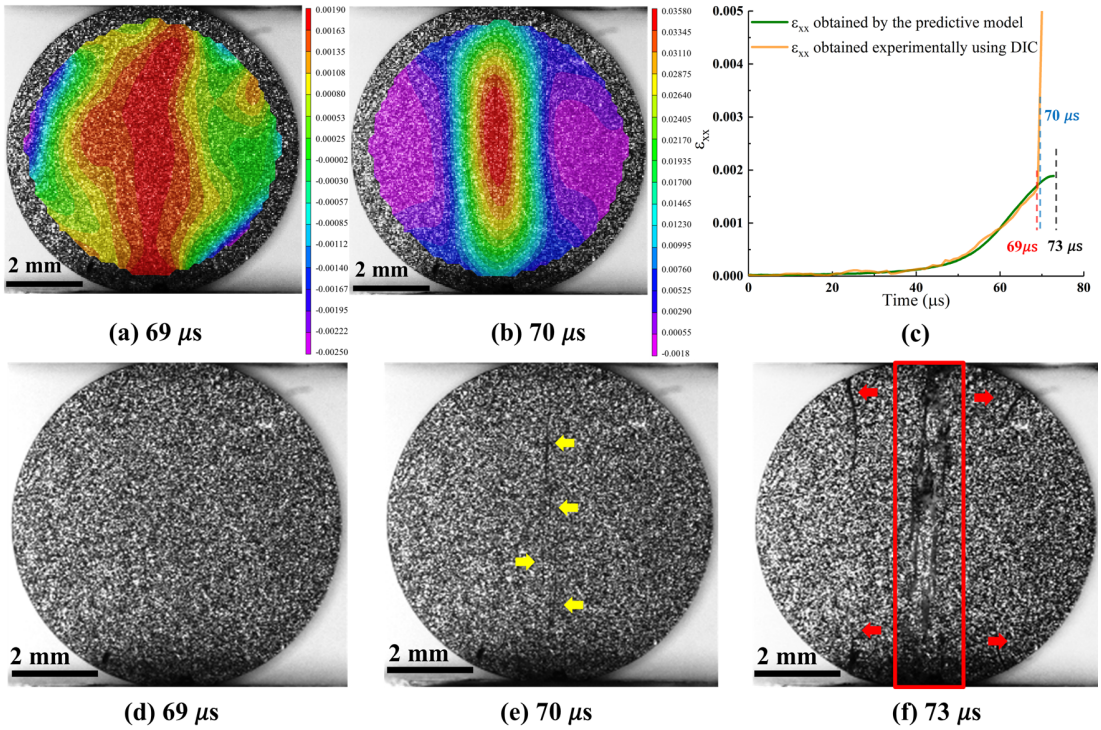

Figure 9: This figure shows the fracture process of the FBD sample in a dynamic test with a loading rate of $\dot{F} = 8.69\times10^8$ N/s. a) and b) are the tensile strain (ε_{xx}) field of the sample at 69 and 70 μs, respectively; c) is the ε_{xx} history curves of the disk's center obtained by DIC and the predictive model, which are from Figure 7a; d), e) and f) are the fracture process of the FBD sample obtained by the ultra-high-speed camera. The yellow arrows in e) are main cracks, and the red arrows in f) are secondary cracks. The fragmentation process is found in the red rectangle zone.

Figure 5 previously showed that the location of the maximum tensile *stress* is at the disk's center, and its value is weakly influenced by the types of loading distribution. However, the types of loading distribution are important for determining the location and the value of the maximum tensile *strain* theoretically. For example, the value of the maximum tensile strain in the uniform loading model is smaller than that in the sinusoidal loading model, and their locations are different, as Figure 8a shows. Thus, the loading configurations (or the types

of loading distribution) should be carefully considered in the dynamic BD tests for advanced ceramics through experimental design (e.g., specimen geometry and/or setup modification) to prevent cracks induced by the maximum tensile strain appearing early and affecting the central crack [15]. According to Figure 8a, applying a uniformly distributed load can better limit the maximum tensile strain. Various efforts have been made in the literature to obtain a uniformly distributed load by experimental methods. For example, Yu et al.[74] designed special spacers with a 20° arc angle to improve the contact between the specimen and spacers in order to generate a uniform stress distribution. In a separate study, Swab et al. [75] placed a piece of grafoil between the specimen and load platens to promote a uniform stress distribution along the contact interface.

3.3. Unraveling structure vs. material failure

Now, we explore the difference between the tensile strength (material failure) and structural failure, especially in the dynamic tests. The current study will still use the crack at the disk's center (the location of the maximum stress) to determine the material's tensile strength of the FBD samples. This is because: 1) the crack at the disk's center based on the Griffith failure criterion is widely accepted and used to determine the tensile strength in the dynamic FBD tests for brittle materials, including advanced ceramics [6, 15, 23, 24, 25, 26]; 2) the location of maximum stress is at the disk's center and is independent of the types of loading distribution (see Figure 5); and 3) the stress and strain at the disk's center is insensitive to the types of loading distribution as the results of the uniform and sinusoidal loading model are the same at the disk's center (see Figure 8). The theoretical results of the uniform and sinusoidal loading models are the same for the disk's center; thus, we can choose either the uniform or sinusoidal loading model (Equations (4) and (7)) to calculate the predictive results (i.e., stress and strain) at the disk's center.

In the dynamic tests, the central crack may occur before the recorded peak stress is reached. Using the peak load to calculate the tensile strength without any correction might lead to overestimating the strength [25, 64]. To avoid the overestimation problem, we define the tensile stress when the central crack first occurs to be the tensile strength of the alumina ceramics. To identify when the central crack first appears, the tensile strain evolution and fracture process are investigated. In addition to the time-resolved images showing the fracture process in the disk,

Figure 9 also includes the temporally-evolving tensile strain of the disk's center (Figure 9c). Here, we observe the tensile strain (ε_{xx}) obtained by DIC analysis is consistent with the results predicted by the model at 69 μs, and no crack is observed on the sample surface as Figure 9d shows. However, at 70 μs in Figure 9c, the tensile strain (ε_{xx}) obtained by the DIC analysis increases rapidly, and the central crack occurs at 70 μs in Figure 9e. Thus, we take the tensile stress $\sigma_{xx} = 320.6$ MPa at 70 μs as the indirect tensile strength with the tensile strain rate of $\dot{\varepsilon} = 91$ s^{-1} for the disk's center. It is observed that the tensile strength is smaller than the peak stress, which occurs at 73 μs, as Figure 9c and Figure 7a show. According to Hooke's law, the predictive tensile strain history is obtained from the loading (or stress) history, and their peak values occur at the same time. In Figure 9f, it can also be observed that the cracks continue to propagate, interact and generate fragments at around 73 μs in the dynamic FBD test. In the literature [64, 76], it has been noted that during the fracture and fragmentation process in the compression loading period, the absorbed energy contributes to the generation of new surfaces, the number and size of fragments, and the kinetic energy of moving fragments. Thus, the peak loading (or stress) at around 73 μs in Figure 9c is related to fracture and fragmentation processes (the structural failure), which is higher than the material tensile strength. The phenomena that the peak loading stress is higher than the material tensile strength has been referred to as the "overloading" phenomena in the literature [25]. Here, we observe that the difference between the peak loading stress and material tensile strength is associated with the time it takes for the fracture to propagate and span the structure during the loading process. In the current study, we define this fracture evolution and fragmentation process happening during the loading process as the "time-dependent structural failure" phenomenon.

Next, we explore the "overloading" phenomenon observed in the experiments with different strain rates. Figure 10 shows four representative examples comparing the predictive strain components with DIC results for the disk's center. Figure 10a and b show that the predictive strain components are consistent with DIC results, and the failure occurs when the peak load is reached in quasi-static tests. The "overloading" phenomena is not observed in the quasi-static loading condition because the fracture and fragmentation processes happen in μs [73], and the "time-dependent structural failure" is extremely short compared with the loading time (e.g., seconds) in the quasi-static tests. Thus, in the quasi-static tests, the "time-dependent structural failure" phenomenon can be reasonably ignored, and we identify the peak stress as

the tensile strength [12, 13]. In the dynamic tests, Figure 10c and d show that there is a rapid increase in the experimentally measured tensile strain prior to the peak stress (or peak predictive strain). The rapid increase in the experimentally measured tensile strain is associated with the "structural-dependent failure", and this process results in the "overloading" phenomena in all the dynamic tests.

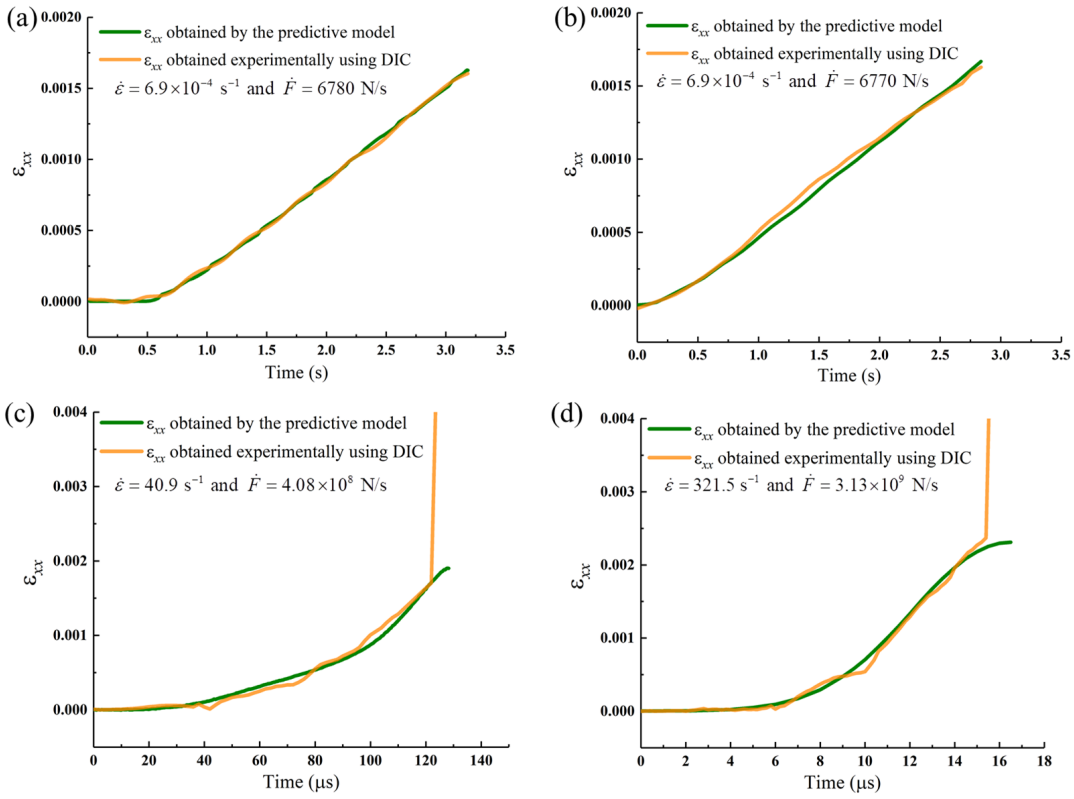

Figure 10: The DIC tensile strain history vs. predictive tensile strain history for the disk's center in the FBD test with various loading rates. The predictive tensile strain history is obtained theoretically using Equations (4) and (7) and Hooke's law. The tensile strain rates $\dot{\varepsilon}$ and loading rates $\dot{F}$ are listed in the legend. In this figure, a) and b) are quasi-static experimental results, and c) and d) are dynamic experimental results.

The disadvantage of this time-matching method to determine the material tensile strength is related to the challenge of determining the delay time between the measured tensile strength and the peak stress. It means this method requires sophisticated data acquisition and ultra-high-speed camera systems. In addition, this method requires the first-appearing crack to be at

the disk center, which means more tests should be performed to satisfy this requirement.

3.4. Strain-rate-dependent tensile strength and post-mortem fractographic analysis

For each strain rate, we run at least three tests, and the variability on experimental results (e.g., the strain rate and tensile strength) is now summarized in Table 1. The experiments include quasi-static and dynamic tests with different pulse shapers (i.e., tin, HDPE and paper) for achieving various strain rates. In Table 1, the strain rate is calculated from the slope of the tensile strain-time history at the disk's center (shown in Figure 7); the loading rate is obtained from the slope of the loading curve (shown in Figure 3); the peak stress at the disk's center is calculated by Equations (4) and (7) which obtain the same results for the disk's center; the material tensile stress is determined by the tensile stress when the central crack first occurs, and its corresponding tensile strain is listed as the "tensile strain when the central crack first appears". In all the quasi-static tests, the peak stress is the same as the material tensile strength without observing the "overloading" phenomenon. However, the "overloading" phenomenon is observed in all dynamic testing leading to tensile strength lower than the peak stress.

Table 1: The experimental results of the FBD tests under different loading rates

	Strain rate (s^{-1})	Loading rate (N/s)	Peak stress (MPa)	Material tensile strength (MPa)	Tensile strain when the central crack first appears
Quasi-static tests	7×10^{-6}	69.9	292.1	292.1	0.00157
	7.8×10^{-5}	755	324.9	324.9	0.00185
	7.8×10^{-5}	754	277.5	277.5	0.00153
	7.5×10^{-5}	738	271.4	271.4	0.00151
	6.9×10^{-4}	6780	321.7	321.7	0.00163
	6.9×10^{-4}	6770	329.8	329.8	0.00171
Dynamic tests (pulse shaper: tin)	40.9	4.08×10^{8}	340.2	324.5	0.00176
	42.1	4.03×10^{8}	332.4	321.2	0.00182
	40.7	4.02×10^{8}	333.3	316.1	0.00171
Dynamic tests (pulse shaper: HDPE)	91.4	8.69×10^{8}	337.8	320.6	0.00179
	71	6.72×10^{8}	357.2	334.1	0.00186
	85.4	8.21×10^{8}	335.1	316.7	0.00169
Dynamic tests (pulse shaper: paper)	321.5	3.13×10^{9}	413.1	399.1	0.00241
	321.7	3.08×10^{9}	383.7	371.3	0.00192
	385.5	3.67×10^{9}	413.4	400.2	0.00252
	387	3.68×10^{9}	395.7	383.7	0.00194

Next, post-mortem fractographic analysis is used to investigate the microstructural fracture mechanisms of the CeramTec 98% alumina under quasi-static and dynamic indirect tension loading. Figure 11a and b show the fracture surfaces taken from quasi-static tests. The rough fracture surface consists of sharp edges, indicating intergranular cracking is the dominant failure mechanism. Intergranular-type fracture has been commonly observed in alumina materials because of the relatively weak interfacial strength [77, 78]. In addition, pores resulting from the impurity phase (e.g., oxide contaminants of Mg, Si and Ca [53]) pullout and cleavages are observed on large flat grain surfaces. For the CeramTec 98% alumina under dynamic loading in Figure 11c and d, the intergranular fractures result in the uneven fracture surface, but more transgranular micro-cracks span across the grains. Besides cleavages and pores, micro-crack branching can be observed in Figure 11d. Overall, the fracture mode transitions from mainly intergranular fracture under quasi-static loading to both intergranular and transgranular fracture under dynamic loading in indirect tension experiments.

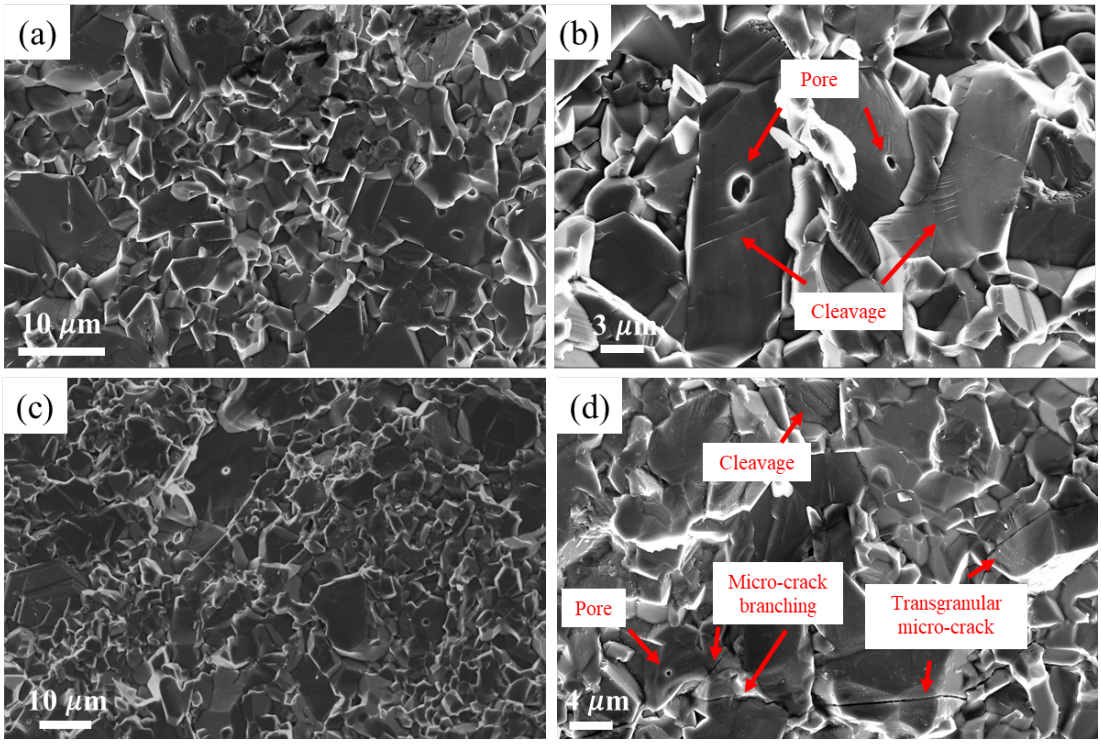

Figure 11: SEM images of the fracture surface of the CeramTec 98% alumina by the indirect tension tests. a) and b) are quasi-static experimental results, where the fracture surface is rough and full of sharp edges, indicating intergranular cracking is the dominant failure mechanism. c) and d) are dynamic experimental results, and the failure process is governed by a mixed-mode of intergranular and transgranular fracture. Pores and cleavages are observed in both quasi-static and dynamic tests.

Figure 12 shows the strain-rate-dependent tensile strength of various alumina ceramics, and the legend lists the testing types, the material names, and the corresponding literature citation. The red points in Figure 12 are the tensile strength of the CeramTec 98% alumina considered in this study under strain rates between 10^{-6} and 400 s^{-1}. It is found that the tensile strength variability is large in the quasi-static tests, and the level of scattering tends to decrease with higher loading rates for the CeramTec 98% alumina. This is because, in quasi-static conditions, the brittle material follows the weakest link hypothesis, and the mechanical properties of the local weakest sites of different samples (e.g., the relatively weak interfacial strength in Figure 11b) are more variable [77, 78, 79]. But in dynamic conditions with higher loading rates, more micro-cracks are nucleated (shown in Figure 11d), which results in a smaller scattering effect

[78, 79, 80]. Figure 12 also shows the tensile strength of other alumina ceramics under different strain rates [44, 46, 49, 50, 51]. Note that most tensile strength values are known, while some are given with the average values and error bars depending on how they were presented in their original publication. The additional alumina ceramics from the literature [44, 46, 49, 50] are manufactured by Morgan Matroc with different purities of 94% (A94), 98% (A98), and 99.5% (A99). From Figure 12, it is observe that the CeramTec 98% alumina has greater tensile strength than other alumina ceramics across all strain rates, especially in the quasi-static tests.

Then, we apply the strain-rate-dependent tensile strength model (Equation (18)) proposed in the current study to the experimental results of the CeramTec 98% alumina and other alumina ceramics [44, 46, 49, 50]. Note that this model is based on the one-dimensional elastic wave theory, and thus, this model is only applicable for the uniaxial tension condition. Although the tensile strength obtained from the FBD or BD experiments in our study are evaluated in a state of biaxial stress, and it is widely accepted that the FBD or BD experimental results can be used as the uniaxial (one-dimensional) tensile strength [44, 46, 49]. In the current study, we also calculate the tensile strength with a correction method to determine the tensile strength as the stress when the central crack first occurs. This tensile strength does not include the fracture propagation and interaction process ("time-dependent structural failure"), which satisfies the "single crack initiation" criteria in the proposed model. The black dash curve in Figure 12 is the strain-rate-dependent tensile strength model for the CeramTec 98% alumina with $\sigma_{cr} = 314$ MPa and $a = 31$ in Equation (18). The black full curve in Figure 12 is the model for the A94, A98 and A99 with $\sigma_{cr} = 181$ MPa and $a = 15$ in Equation (18). It is observed that the tensile strength at lower strain rates remains nearly constant, and its value equals to σ_{cr}. When the strain rate is higher than a static-dynamic transition strain rate [81], the tensile strength will increase rapidly, as has also been observed in other models [82, 83]. The transition strain rates of the different alumina ceramics are discussed later in this section.

Next, it is observed that there are some differences between the proposed model for A94, A98 and A99 and the values measured at high strain rates in Figure 12. First, this is because the model is fitted to all three types of alumina ceramics, with each ceramic having a different microstructure, purity, and expected material properties based on these differences [82, 84]. Second, their strengths are determined by two kinds of experiments (i.e., dynamic Brazilian disk tests at a strain rate of around 40 s^{-1} and spall tests at a strain rate of around 1000 s^{-1}). In

the dynamic Brazilian disk tests, the "overloading" phenomenon may lead to an overestimation of the tensile strength at around 40 s^{-1}, which explains that the experimental data is higher than our model. For the spall tests at around 1000 s^{-1}, the elastic wave dispersion in cylindrical rods (e.g., material dispersion and geometrical dispersion) may cause the decrease of the peak pulse observed in a typical spall test of a ceramic material [85]. Furthermore, microstructural effects [44] will also manifest differently between the Brazilian disk and spall tests given they are performed under different stress states. The data denoted by the red dashed rectangle in Figure 12 lie outside of the model prediction because their strengths are lower than those of the same material at a lower strain rate. These data are still included in the Figure 12 for completeness. Overall, the proposed model is mostly consistent with experimental results from the current study and the literature [44, 46, 49, 50, 51].

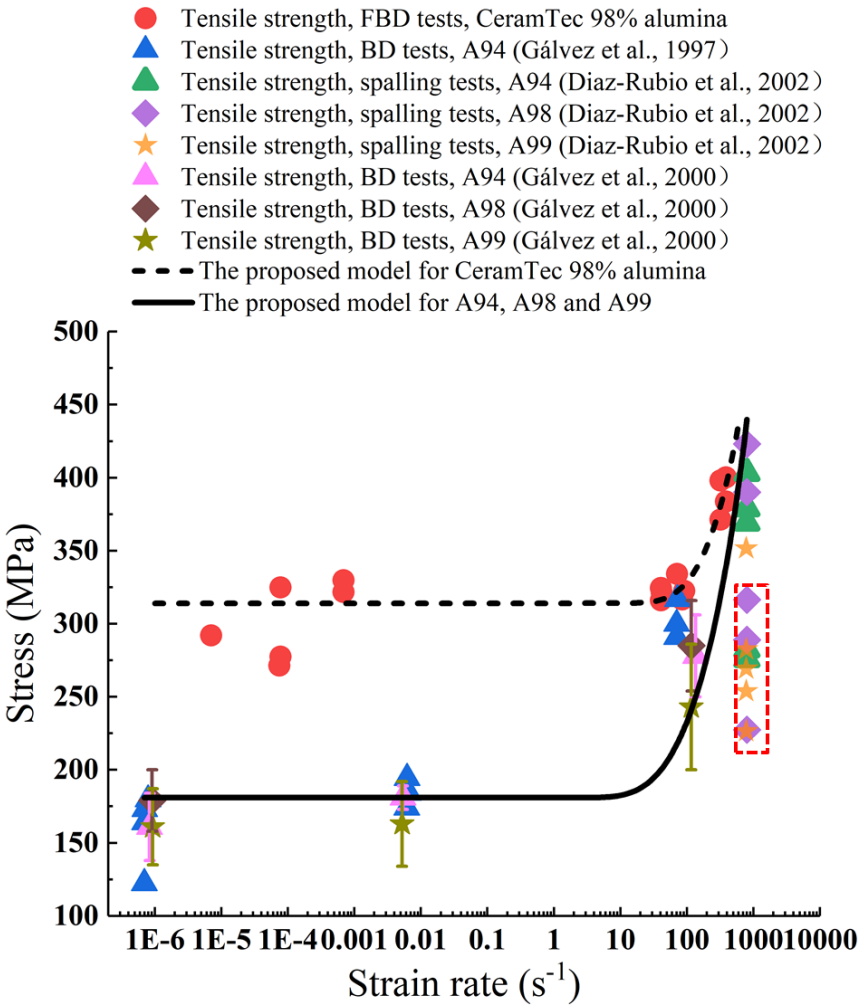

Figure 12: Strain-rate-dependent tensile strength of various alumina ceramics. The red points are the material tensile strength of the CeramTec 98% alumina studied here. The other colored points are the tensile strength of different alumina obtained from literature [44, 46, 49, 50, 51]. The legend includes the testing types, the material names, and the corresponding literature citation. The black dash curve in the figure is the strain-rate-dependent tensile strength model for the CeramTec 98% alumina with $\sigma_{cr} = 314$ MPa and $a = 31$ in Equation (18). The black full curve in the figure is the model for the A94, A98 and A99 with $\sigma_{cr} = 181$ MPa and $a = 15$ in Equation (18). A red dash rectangle is used to denote some data because their strengths are lower than those of the same material at a lower strain rate. These data lie outside the model prediction but are still included in the figure for completeness.

To describe the strain-rate-dependent tensile behavior of alumina ceramics in a general form,

the tensile strength σ_0 in Equation (18) is normalized by the characteristic stress σ_{cr} and the applied strain rate $\dot{\varepsilon}$ by the characteristic factor a^2:

$$\sigma_0^* = \frac{e^{\dot{\varepsilon}_*^{-0.5}}}{e^{\dot{\varepsilon}_*^{-0.5}} - 1} \tag{19}$$

with

$$\sigma_0^* = \frac{\sigma_0}{\sigma_{cr}}, \dot{\varepsilon}_* = \frac{\dot{\varepsilon}}{a^2} \tag{20}$$

Figure 13 describes the strain-rate-dependent tensile behavior of all alumina ceramics in the normalized form. The black curve in Figure 13 is the normalized strain-rate-dependent tensile strength model for alumina ceramics obtained by Equation (19). The colored points are the normalized tensile strength of various alumina ceramics with different normalized strain rates obtained from experiments [44, 46, 49, 50, 51]. Broadly, it is observed that the normalized tensile strength of alumina ceramics would remain nearly constant below a transition strain rate (around $\dot{\varepsilon} = 0.04a^2$), while a rapid increase in strength develops as the strain rate increases above the transition strain rate. The transition strain rate for the CeramTec 98% alumina is around 39 s^{-1}, and is around 9 s^{-1} for the A94, A98, and A99 alumina. According to Equation (20) and Figure 13, the alumina becomes more rate sensitive when the transition strain rate ($0.04a^2$) is smaller. Thus, a is the factor associated with the strain rate sensitivity of the materials, and the CeramTec 98% alumina shows less rate sensitivity than the other alumina ceramics (i.e., A94, A98 and A99). Overall, this model can describe the strain-rate-dependent tensile behavior of alumina ceramics in a general form, and this has implications if one wanted to implement such strain-rate-dependent tensile model into higher scale constitutive models (e.g., Johnson–Holmquist–Beissel model [86]).

Finally, the limitations of this strain-rate-dependent tensile strength model are that the model is only applicable for the uniaxial tension condition, and the tensile failure should satisfy the "single crack initiation" criteria. In addition, this model does not consider temperature effects and cannot be applied to higher strain rate experiments (e.g., laser shock tests).

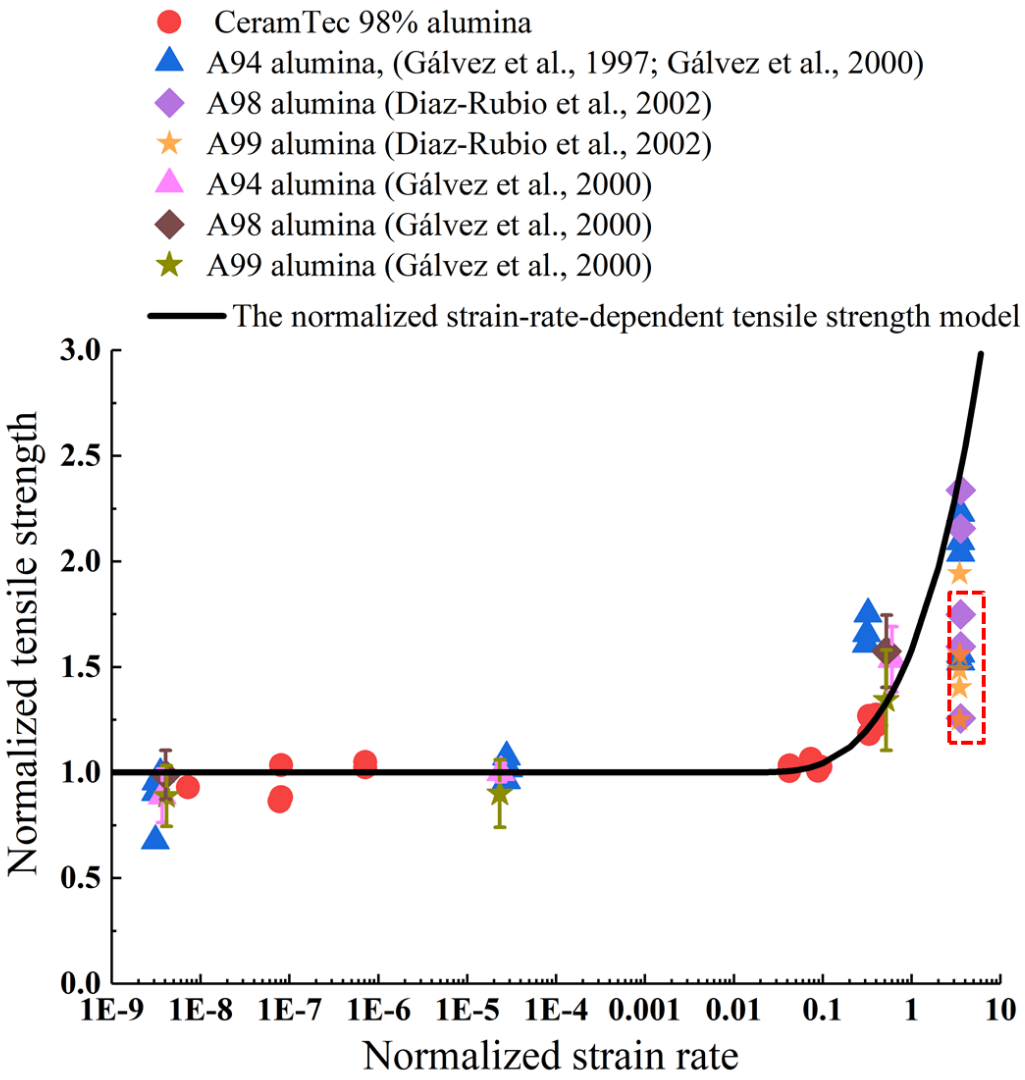

Figure 13: The relationship between the normalized tensile strength and normalized strain rates of various alumina ceramics. The black curve is the normalized strain-rate-dependent tensile strength model obtained by Equation (19). The red points are the normalized tensile strength of the CeramTec 98% alumina. The other colored points are the normalized tensile strength of different alumina obtained from literature [44, 46, 49, 50, 51]. The experimental data is normalized by Equation (20). A red dash rectangle is used to denote some data because their strengths are lower than those of the same material at a lower strain rate. These data lie outside the model prediction but are still included in the figure for completeness.

4. Conclusion

In this study, experimental and modelling methods are used to investigate the strain-rate-dependent tensile response of an alumina ceramic. Several key outcomes are obtained:

1. The locations of maximum tensile stress and maximum tensile strain are different along the compressive diametral line, and the loading distribution affects both the value and location of the maximum tensile strain along the vertical diameter, but has little influence on the area near the disk's center where the maximum tensile stress occurs;

2. In the dynamic tests, multiple cracks appear simultaneously around the locations of maximum tensile stress and strain, and this observation means that the splitting fracture of a Brazilian disk may not be controlled only by the Griffith failure criterion (the maximum tensile stress), but also by the maximum tensile strain;

3. In the dynamic tests, cracks appear prior to the recorded peak load, and the peak stress corresponding to the failure of the sample structure is different from the tensile strength of the material, which is referred to as the "overloading" phenomenon;

4. The difference between the peak stress and material tensile strength is associated with the time it takes for the crack to propagate, interact, and span the structure during the loading process, which is referred to as "time-dependent structural failure";

5. The strain-rate-dependent tensile strength of the alumina ceramics is achieved with a correction method, which is determined by the tensile stress when the central crack first occurs;

6. The fracture mode transitions from mainly intergranular fracture under quasi-static loading conditions to both intergranular and transgranular fracture under dynamic loading in indirect tension experiments.

7. A strain-rate-dependent tensile strength model for alumina ceramics is proposed based on one-dimensional elastic wave theory, the Griffith failure criterion, and experimental observations. This model is consistent with the experimental results of the CeramTec 98% and other alumina ceramics (i.e., A94, A98 and A99).

5. Acknowledgment

This work is supported by Defence Research and Development Canada (DRDC), General Dynamics Land Systems–Canada, and NP Aerospace through NSERC Alliance project ALLRP 560447-2020. The views and conclusions contained in this document are those of the authors and should not be interpreted as representing the official policies, either expressed or implied, of General Dynamics, NP Aerospace, DRDC or the Government of Canada. The Government of Canada is authorized to reproduce and distribute reprints for Government purposes notwithstanding any copyright notation herein.

References

[1] M. Anglada, Assessment of mechanical properties of ceramic materials, in: Advances in Ceramic Biomaterials, Elsevier, 2017, pp. 83–109.

[2] M. Scapin, L. Peroni, M. Avalle, Dynamic brazilian test for mechanical characterization of ceramic ballistic protection, Shock and Vibration 2017 (2017).

[3] E. Medvedovski, Ballistic performance of armour ceramics: Influence of design and structure. part 1, Ceramics International 36 (7) (2010) 2103–2115.

[4] J. Langford, M. A. Perras, Obtaining reliable estimates of intact tensile strength, in: 48th US Rock Mechanics/Geomechanics Symposium, OnePetro, 2014.

[5] Y. Dai, Y. Li, X. Xu, Q. Zhu, W. Yan, S. Jin, H. Harmuth, Fracture behaviour of magnesia refractory materials in tension with the brazilian test, Journal of the European Ceramic Society 39 (16) (2019) 5433–5441.

[6] L. Zhang, D. Townsend, N. Petrinic, A. Pellegrino, Loading mode and lateral confinement dependent dynamic fracture of a glass ceramic macor, Journal of Dynamic Behavior of Materials (2022) 1–18.

[7] Z. Bieniawski, I. Hawkes, Suggested methods for determining tensile strength of rock materials, Int J Rock Mech Min Sci Geomech Abstr 15 (3) (1978) 99–103.

[8] A. Brückner-Foit, T. Fett, D. Munz, K. Schirmer, Discrimination of multiaxiality criteria with the brazilian disc test, Journal of the European Ceramic Society 17 (5) (1997) 689–696.

[9] ASTM C496-11, Standard test method for splitting tensile strength of cylindrical concrete specimens (2011).

[10] Y. Belrhiti, J. Dupre, O. Pop, A. Germaneau, P. Doumalin, M. Huger, T. Chotard, Combination of brazilian test and digital image correlation for mechanical characterization of refractory materials, Journal of the European Ceramic Society 37 (5) (2017) 2285–2293.

[11] J. Li, J. Zhao, H. Wang, K. Liu, Q. Zhang, Fracturing behaviours and ae signatures of anisotropic coal in dynamic brazilian tests, Engineering Fracture Mechanics 252 (2021) 107817.

[12] Q.-Z. Wang, L. Xing, Determination of fracture toughness kic by using the flattened brazilian disk specimen for rocks, Engineering fracture mechanics 64 (2) (1999) 193–201.

[13] Q.-Z. Wang, L. Wu, The flattened brazilian disc specimen used for determining elastic modulus, tensile strength and fracture toughness of brittle rocks: experimental results, International Journal of Rock Mechanics and Mining Sciences 41 (2004) 26–30.

[14] Q.-Z. Wang, X. Jia, S. Kou, Z. Zhang, P.-A. Lindqvist, The flattened brazilian disc specimen used for testing elastic modulus, tensile strength and fracture toughness of brittle rocks: analytical and numerical results, International Journal of Rock Mechanics and Mining Sciences 41 (2) (2004) 245–253.

[15] Q.-Z. Wang, W. Li, H. Xie, Dynamic split tensile test of flattened brazilian disc of rock with SHPB setup, Mechanics of Materials 41 (3) (2009) 252–260.

[16] J. Antonn, A. Rajendran, Effect of strain rate and size on tensile strength of concrete, in: Proceedings of the topical conference on shock compression of condensed matter. Elsevier, Amsterdam, Vol. 501, 1992.

[17] R. John, T. Antoun, A. Rajendran, Effect of strain rate and size on tensile strength of concrete, in: Shock Compression of Condensed Matter–1991, Elsevier, 1992, pp. 501–504.

[18] S. Dong, K. Xia, S. Huang, T. Yin, Rate dependence of the tensile and flexural strengths of glass–ceramic macor, Journal of Materials Science 46 (2) (2011) 394–399.

[19] Y. Zhou, K.-w. Xia, X. Li, H.-B. Li, G. Ma, J. Zhao, Z. Zhou, F. Dai, Suggested methods for determining the dynamic strength parameters and mode-i fracture toughness of rock materials, in: The ISRM Suggested Methods for Rock Characterization, Testing and Monitoring: 2007-2014, Springer, 2011, pp. 35–44.

[20] J. D. Hogan, J. Kimberley, K. Hazeli, J. Plescia, K. Ramesh, Dynamic behavior of an ordinary chondrite: The effects of microstructure on strength, failure and fragmentation, Icarus 260 (2015) 308–319.

[21] M. R. Khosravani, K. Weinberg, A review on split Hopkinson bar experiments on the dynamic characterisation of concrete, Construction and Building Materials 190 (2018) 1264–1283.

[22] S. Cao, E. Yilmaz, W. Song, Dynamic response of cement-tailings matrix composites under shpb compression load, Construction and Building Materials 186 (2018) 892–903.

[23] X. Chen, S. Wu, J. Zhou, Quantification of dynamic tensile behavior of cement-based materials, Construction and Building Materials 51 (2014) 15–23.

[24] A. Elghazel, R. Taktak, J. Bouaziz, Investigation of mechanical behaviour of a bioceramic, Fracture Mechanics: Properties, Patterns and Behaviours (2016) 277.

[25] M. R. Khosravani, M. Silani, K. Weinberg, Fracture studies of ultra-high performance concrete using dynamic brazilian tests, Theoretical and Applied Fracture Mechanics 93 (2018) 302–310.

[26] P. Chen, B. Guo, J. Chen, Comparative study of the dynamic fracture toughness determination of brittle materials using the kolsky-hopkinson bar machine, in: The Kolsky-Hopkinson Bar Machine, Springer, 2018, pp. 143–156.

[27] Z. Yan, F. Dai, Y. Liu, M. Wei, W. You, New insights into the fracture mechanism of flattened brazilian disc specimen using digital image correlation, Engineering Fracture Mechanics 252 (2021) 107810.

[28] M. Mellor, I. Hawkes, Measurement of tensile strength by diametral compression of discs and annuli, Engineering Geology 5 (3) (1971) 173–225.

[29] H. Schuler, C. Mayrhofer, K. Thoma, Spall experiments for the measurement of the tensile strength and fracture energy of concrete at high strain rates, International Journal of Impact Engineering 32 (10) (2006) 1635–1650.

[30] P. Colback, An analysis of brittle fracture initiation and propagation in the brazilian test, in: 1st ISRM Congress, OnePetro, 1966.

[31] D. Li, L. N. Y. Wong, The brazilian disc test for rock mechanics applications: review and new insights, Rock mechanics and rock engineering 46 (2) (2013) 269–287.

[32] C. F. Markides, D. Pazis, S. Kourkoulis, Closed full-field solutions for stresses and displacements in the brazilian disk under distributed radial load, International Journal of Rock Mechanics and Mining Sciences 47 (2) (2010) 227–237.

[33] N. Erarslan, Z. Z. Liang, D. J. Williams, Experimental and numerical studies on determination of indirect tensile strength of rocks, Rock Mechanics and Rock Engineering 45 (5) (2012) 739–751.

[34] G. Hondros, The evaluation of poisson's ratio and the modulus of materials of low tensile resistance by the brazilian (indirect tensile) test with particular reference to concrete, Australian J. Appl. Sci. 10 (3) (1959) 243–268.

[35] B. Amadei, Importance of anisotropy when estimating and measuring in situ stresses in rock, in: International journal of rock mechanics and mining sciences & geomechanics abstracts, Vol. 33, Elsevier, 1996, pp. 293–325.

[36] C.-S. Chen, E. Pan, B. Amadei, Determination of deformability and tensile strength of anisotropic rock using brazilian tests, International Journal of Rock Mechanics and Mining Sciences 35 (1) (1998) 43–61.

[37] P. Pandey, D. Singh, Deformation of a rock in different tensile tests, Engineering geology 22 (3) (1986) 281–292.

[38] R. Nova, A. Zaninetti, An investigation into the tensile behaviour of a schistose rock, in: International Journal of rock mechanics and mining sciences & geomechanics abstracts, Vol. 27, Elsevier, 1990, pp. 231–242.

[39] C. F. Markides, D. Pazis, S. Kourkoulis, The brazilian disc under non-uniform distribution of radial pressure and friction, International Journal of Rock Mechanics and Mining Sciences 50 (2012) 47–55.

[40] C. F. Markides, S. Kourkoulis, The stress field in a standardized brazilian disc: the influence of the loading type acting on the actual contact length, Rock Mechanics and Rock Engineering 45 (2) (2012) 145–158.

[41] S. Okubo, K. Fukui, Complete stress-strain curves for various rock types in uniaxial tension, in: International journal of rock mechanics and mining sciences & geomechanics abstracts, Vol. 33, Elsevier, 1996, pp. 549–556.

[42] T. Stacey, A simple extension strain criterion for fracture of brittle rock, in: International Journal of Rock Mechanics and Mining Sciences & Geomechanics Abstracts, Vol. 18, Elsevier, 1981, pp. 469–474.

[43] S. P. Timoshenko, J. N. Goodier, Theory of elasticity (1951).

[44] F. G. Dıaz-Rubio, J. R. Perez, V. S. Gálvez, The spalling of long bars as a reliable method of measuring the dynamic tensile strength of ceramics, International Journal of Impact Engineering 27 (2) (2002) 161–177.

[45] W. W. Chen, B. Song, Split Hopkinson (Kolsky) bar: design, testing and applications, Springer Science & Business Media, 2010.

[46] F. Gálvez, J. Rodríguez, V. S. Gálvez, A wave propagation technique to measure the dynamic tensile strength of brittle materials, Le Journal de Physique IV 10 (PR9) (2000) Pr9–203.

[47] X. Li, M. Tao, C. Wu, K. Du, Q. Wu, Spalling strength of rock under different static pre-confining pressures, International Journal of Impact Engineering 99 (2017) 69–74.

[48] H. Zhao, M. Tao, X. Li, W. Cao, C. Wu, Estimation of spalling strength of sandstone under different pre-confining pressure by experiment and numerical simulation, International Journal of Impact Engineering 133 (2019) 103359.

[49] F. Gálvez, J. Rodriguez, V. Sánchez, Tensile strength measurements of ceramic materials at high rates of strain, Le Journal de Physique IV 7 (C3) (1997) C3–151.

[50] F. Gálvez, J. Rodríguez, V. S. Gálvez, Influence of the strain rate on the tensile strength in aluminas of different purity, Le Journal de Physique IV 10 (PR9) (2000) Pr9–323.

[51] J. Chen, B. Guo, H. Liu, H. Liu, P. Chen, Dynamic brazilian test of brittle materials using the split hopkinson pressure bar and digital image correlation, Strain 50 (6) (2014) 563–570.

[52] K. KMW, Ceramic materials for light-weight ceramic polymer armor systems.

[53] J. Zheng, M. Ji, Z. Zaiemyekeh, H. Li, J. D. Hogan, Strain-rate-dependent compressive and compression-shear response of an alumina ceramic, Journal of the European Ceramic Society 42 (2022) 7516–7527.

[54] M. Ji, H. Li, J. Zheng, S. Yang, Z. Zaiemyekeh, J. D. Hogan, An experimental study on the strain-rate-dependent compressive and tensile response of an alumina ceramic, Ceramics International 48 (19) (2022) 28121–28134.

[55] F. Dai, S. Huang, K. Xia, Z. Tan, Some fundamental issues in dynamic compression and tension tests of rocks using split hopkinson pressure bar, Rock mechanics and rock engineering 43 (6) (2010) 657–666.

[56] D. Hobbs, The tensile strength of rocks, in: International Journal of Rock Mechanics and Mining Sciences & Geomechanics Abstracts, Vol. 1, Elsevier, 1964, pp. 385–396.

[57] B. M. Koch, P. Jannotti, D. Mallick, B. Schuster, T. Sano, J. D. Hogan, Influence of microstructure on the impact failure of alumina, Materials Science and Engineering: A 770 (2020) 138549.

[58] C. Lo, H. Li, G. Toussaint, J. D. Hogan, On the evaluation of mechanical properties and ballistic performance of two variants of boron carbide, International Journal of Impact Engineering 152 (2021) 103846.

[59] J. Gomez, A. Shukla, A. Sharma, Static and dynamic behavior of concrete and granite in tension with damage, Theoretical and Applied Fracture Mechanics 36 (1) (2001) 37–49.

[60] H. Kolsky, An investigation of the mechanical properties of materials at very high rates of loading, Proceedings of the physical society. Section B 62 (11) (1949) 676.

[61] H. Kolsky, Stress waves in solids. dover books on physics, new york (1963).

[62] G. Ravichandran, G. Subhash, Critical appraisal of limiting strain rates for compression testing of ceramics in a split hopkinson pressure bar, Journal of the American Ceramic Society 77 (1) (1994) 263–267.

[63] L. Zhang, A. Pellegrino, D. Townsend, N. Petrinic, Strain rate and temperature dependent strain localization of a near α titanium alloy, International Journal of Impact Engineering 145 (2020) 103676.

[64] Q. B. Zhang, J. Zhao, A review of dynamic experimental techniques and mechanical behaviour of rock materials, Rock mechanics and rock engineering 47 (4) (2014) 1411–1478.

[65] H. Li, C. Shao, D. F. Rojas, M. Ponga, J. D. Hogan, Micro-hardness and strain-rate-dependent compressive response of an ultra-light-weight Mg-Li-Al alloy, Journal of Alloys and Compounds 890 (2022) 161703.

[66] H. Li, P. Motamedi, J. Hogan, Characterization and mechanical testing on novel (γ+ α2)–TiAl/Ti3Al/Al2O3 cermet, Materials Science and Engineering: A 750 (2019) 152–163.

[67] N. Erarslan, D. J. Williams, Experimental, numerical and analytical studies on tensile strength of rocks, International Journal of Rock Mechanics and Mining Sciences 49 (2012) 21–30.

[68] J. T. Gomez, A. Shukla, A. Sharma, Photoelastic evaluation of stress fields and fracture during dynamic splitting experiments, Journal of testing and evaluation 30 (3) (2002) 186–196.

[69] C. Y. Rena, G. Ruiz, A. Pandolfi, Numerical investigation on the dynamic behavior of advanced ceramics, Engineering Fracture Mechanics 71 (4-6) (2004) 897–911.

[70] H. Späth, Mathematical algorithms for linear regression, Academic Press, 2014.

[71] M. J. Pérez-Martín, B. Erice, D. Cendón, F. Gálvez, Spalling uniaxial strength of al2o3 at high strain rates, The European Physical Journal Special Topics 206 (1) (2012) 117–128.

[72] J. J. Swab, C. S. Meredith, D. T. Casem, W. R. Gamble, Static and dynamic compression strength of hot-pressed boron carbide using a dumbbell-shaped specimen, Journal of Materials Science 52 (17) (2017) 10073–10084.

[73] W. D. Neal, G. J. Appleby-Thomas, G. S. Collins, Meso-scopic deformation in brittle granular materials, in: Journal of Physics: Conference Series, Vol. 500, IOP Publishing, 2014, p. 112047.

[74] Y. Yu, J. Zhang, J. Zhang, A modified brazilian disk tension test, International journal of rock mechanics and mining sciences 46 (2) (2009) 421–425.

[75] J. J. Swab, J. Yu, R. Gamble, S. Kilczewski, Analysis of the diametral compression method for determining the tensile strength of transparent magnesium aluminate spinel, International journal of fracture 172 (2) (2011) 187–192.

[76] J. D. Hogan, R. J. Rogers, J. G. Spray, S. Boonsue, Dynamic fragmentation of granite for impact energies of 6–28 j, Engineering Fracture Mechanics 79 (2012) 103–125.

[77] M. Aswad, T. Marrow, Intergranular crack nuclei in polycrystalline alumina, Engineering Fracture Mechanics 95 (2012) 29–36.

[78] Z. Wang, P. Li, Dynamic failure and fracture mechanism in alumina ceramics: Experimental observations and finite element modelling, Ceramics International 41 (10) (2015) 12763–12772.

[79] F. Hild, C. Denoual, P. Forquin, X. Brajer, On the probabilistic–deterministic transition involved in a fragmentation process of brittle materials, Computers & Structures 81 (12) (2003) 1241–1253.

[80] G. Subhash, G. Ravichandran, Split-Hopkinson pressure bar testing of ceramics., Materials Park, OH: ASM International, 2000. (2000) 497–504.

[81] Z. Wang, P. Li, Characterisation of dynamic behaviour of alumina ceramics: evaluation of stress uniformity, AIP Advances 5 (10) (2015) 107224.

[82] J. Kimberley, K. Ramesh, N. Daphalapurkar, A scaling law for the dynamic strength of brittle solids, Acta Materialia 61 (9) (2013) 3509–3521.

[83] C. Dascalu, Dynamic damage law with fragmentation length: strain-rate sensitivity of the tensile response, Journal of Dynamic Behavior of Materials 7 (1) (2021) 156–160.

[84] J. D. Hogan, L. Farbaniec, T. Sano, M. Shaeffer, K. Ramesh, The effects of defects on the uniaxial compressive strength and failure of an advanced ceramic, Acta Materialia 102 (2016) 263–272.

[85] T. G. del Río, J. R. Pérez, Elastic wave propagation in cylindrical bars after brittle failures: Application to spalling tests, International journal of impact engineering 34 (2) (2007) 377–393.

[86] G. R. Johnson, T. J. Holmquist, S. R. Beissel, Response of aluminum nitride (including a phase change) to large strains, high strain rates, and high pressures, Journal of Applied Physics 94 (3) (2003) 1639–1646.